Hydrodynamics of a bathymetrically complex fringing coral reef embayment: Wave climate, in situ observations, and wave prediction

Ron Hoeke,[1,2,3] Curt Storlazzi,[4] and Peter Ridd[3]

Received 4 February 2010; revised 11 January 2011; accepted 27 January 2011; published 20 April 2011.

[1] This paper examines the relationship between offshore wave climate and nearshore waves and currents at Hanalei Bay, Hawaii, an exposed bay fringed with coral reefs. Analysis of both offshore in situ data and numerical hindcasts identify the predominance of two wave conditions: a mode associated with local trade winds and an episodic pattern associated with distant source long-period swells. Analysis of 10 months of in situ data within the bay show that current velocities are up to an order of magnitude greater during long-period swell episodes than during trade wind conditions; overall circulation patterns are also fundamentally different. The current velocities are highly correlated with incident wave heights during the swell episodes, while they are not during the modal trade wind conditions. A phase-averaged wave model was implemented with the dual purpose of evaluating application to bathymetrically complex fringing reefs and to examine the propagation of waves into the nearshore in an effort to better explain the large difference in observed circulation during the two offshore wave conditions. The prediction quality of this model was poorer for the episodic condition than for the lower-energy mode, however, it illustrated how longer-period swells are preferentially refracted into the bay and make available far more nearshore wave energy to drive currents compared to waves during modal conditions. The highly episodic circulation, the nature of which is dependent on complex refraction patterns of episodic, long-period swell has implications for flushing and sediment dynamics for incised fringing reef-lined bays that characterize many high islands at low latitudes around the world.

Citation: Hoeke, R., C. Storlazzi, and P. Ridd (2011), Hydrodynamics of a bathymetrically complex fringing coral reef embayment: Wave climate, in situ observations, and wave prediction, *J. Geophys. Res.*, *116*, C04018, doi:10.1029/2010JC006170
.

1. Introduction

[2] Hydrodynamic forcing of reef systems controls or strongly influences many ecological aspects of the reef, such as patterns of sedimentation and pollutant dispersal, nutrient uptake, dispersal and recruitment of larvae, patterns of coral bleaching, and degree of disturbance due to episodic storms [*Hamner and Wolanski*, 1988; *Andrews and Pickard*, 1990; *Hearn*, 1999; *Madin and Connolly*, 2006]. The importance of surface gravity waves to reef hydrodynamics was identified fairly early [*Munk and Sargent*, 1954; *von Arx*, 1954], and more recent studies have highlighted their dominant contribution for many different reef morphologies [e.g., *Callaghan et al.*, 2006; *Coronado et al.*, 2007; *Hench et al.*, 2008; *Monismith*, 2007]. Additionally, distribution of wave-generated bed shear stresses have been shown to be the pivotal factor in determining benthic community composition, particularly in wave-dominated areas [e.g., *Dollar*, 1982; *Rogers*, 1993; *Grigg*, 1998; *Fulton and Bellwood*, 2005; *Storlazzi et al.*, 2005]. Most coral reef hydrodynamics studies to date have focused on more linear/barrier reef-lagoon type morphologies, are of too short a duration to capture seasonal changes in circulation, or both [e.g., *Kraines et al.*, 1998; *Storlazzi et al.*, 2004; *Hench et al.*, 2008; *Lowe et al.*, 2009].

[3] In this study, the importance of wave forcing to the hydrodynamics of an open-mouthed bay bordered by fringing coral reefs, a common morphology on tropical and subtropical high islands worldwide, was examined by identifying fundamental differences in the magnitude of flow and overall circulation patterns associated with the two most common offshore wave conditions. These offshore wave conditions are identified through examination of wave climate, defined here by offshore buoy data and numerical hindcasts.

[1]Joint Institute for Marine and Atmospheric Research, University of Hawai'i at Mānoa, Honolulu, Hawaii, USA.
[2]NOAA Pacific Islands Fisheries Science Center, Honolulu, Hawaii, USA.
[3]School of Engineering and Physical Sciences, James Cook University, Townsville, Queensland, Australia.
[4]Coastal and Marine Geology Program, U.S. Geological Survey, Santa Cruz, California, USA.

0148-0227/11/2010JC006170

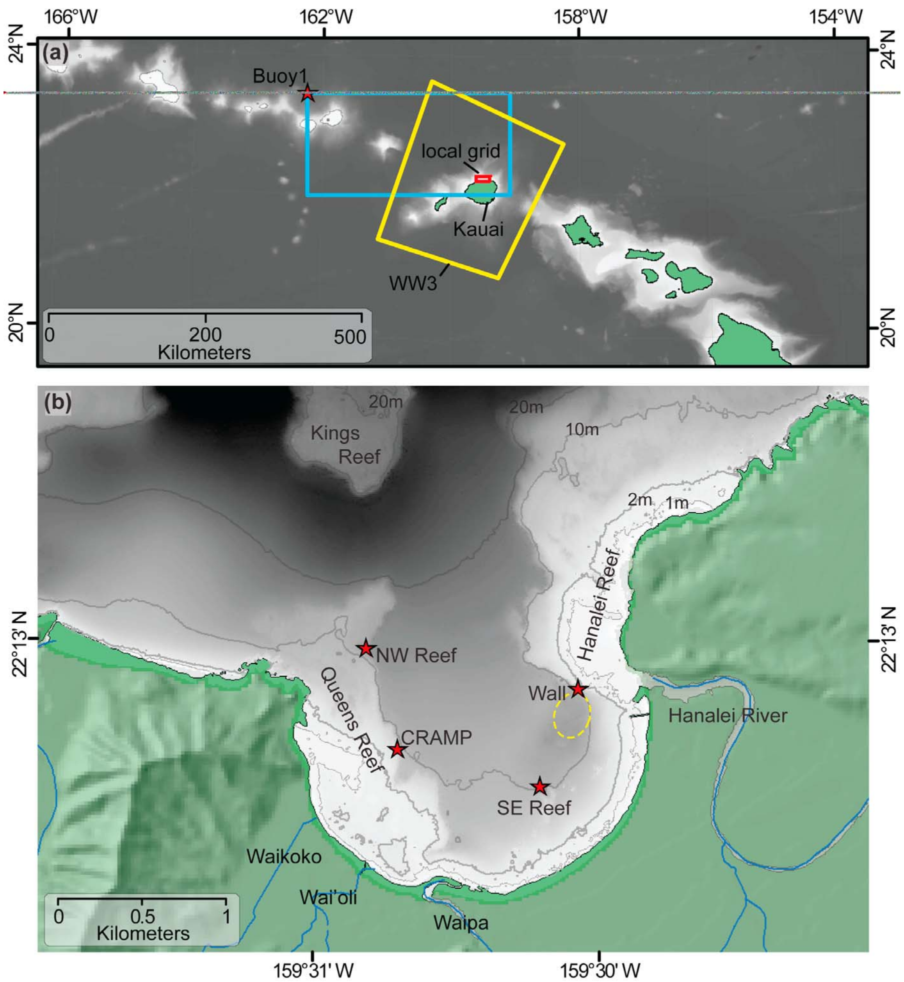

Figure 1. Study site location maps: (a) Hawaiian Archipelago with the position of NOAA NDBC buoy 51001 indicated by a star at the northwest corner of the buoy 1 input grid boundaries (blue). The WW3 input grid boundaries surround the island of Kauai (yellow); the local model grid boundaries are centered on Hanalei Bay on the north coast of Kauai (red). (b) Hanalei Bay with Wall, SE Reef, CRAMP, and NW Reef mooring site positions and bathymetric contours indicated; the mouth of Hanalei River is on the east side of the bay and the Waipa, Wai'ole, and Waikoko streams are indicated. The "Black Hole," outlined with a dotted yellow line, is just south of the Wall site.

A 10 month period of in situ wave and current data is used to identify the nearshore circulation response. The observed differences in circulation are linked to differences in the amount of wave energy propagating into the bay relative to offshore wave energy. Episodic circulation events occur when episodically high wave energy propagates into the bay.

[4] Also in this paper, the performance of the third-generation phase-averaged wave model (SWAN) [*Booij et al.*, 1999] was investigated to determine whether it can be used as a tool to predict wavefield transformation over steep, complex, and hydrodynamically rough bathymetry of open fringing reef bays. Testing the model's ability to predict the shallow water wave processes of propagation, refraction, and diffraction are a necessary precursor to numerical circulation modeling of this type of coastal morphology. The model's ability to predict dissipation due to depth-induced breaking is not evaluated in this paper, as it could not be directly inferred from the observations of wave characteristics (e.g., no linear transect of wave observations across the reef slope and crest was available). This is primarily due to restrictions on instrument deployment locations imposed by the bay's complex fringing reef topography and exceptionally high episodic wave heights. Therefore, inferences of wave dissipation must be made through an analysis of current observations using a coupled circulation model. Because of the complexity of modeled relationships between wave dissipation and resulting current fields, for brevity, this work is not included here, but is addressed in a future paper. The modeled propagation of wave energy into the bay prior to breaking presented here does provide valuable a priori insight into the mechanisms driving the fundamental differences in current magnitudes and circulation patterns observed during the two dominant offshore wave conditions.

[5] The study site, Hanalei Bay on the Hawaiian Island of Kauai (Figure 1), receives a high episodic sediment load from its steep-sided watersheds, and episodic wave events have been identified as important to the distribution, (re) suspension, and transport of these sediments [*Calhoun et al.*,

2002; *Draut et al.*, 2009; *Storlazzi et al.*, 2009]. Such sedimentation has the potential to significantly impact reef ecosystems [*Fabricius*, 2005] and has been implicated in the major ecological degradation of a number of qualitatively similar linked watershed-fringing reef/watershed systems [*Wolanski et al.*, 2003]. This makes understanding flushing mechanisms an imperative for good governance of the bay's ecological resources.

2. Methods

2.1. Study Area Description

[6] Kauai (22.2°N, 159.5°W) is a subtropical high island of volcanic origin lying in the North Pacific trade wind belt. Tides in the area are mixed semidiurnal with neap ranges of around 0.4 m and spring ranges around 0.9 m [*Storlazzi et al.*, 2009]. Trade wind conditions associated with the North Pacific subtropical anticyclone prevail; these winds are typically around 5–12 m/s and generate wind waves generally 1–3 m in height with 6–10 s periods from the east to northeast [*Moberly and Chamberlain*, 1964]. Trade winds occur throughout the year, but are most prevalent during the spring and summer months. Hanalei Bay, approximately 2 km wide, is located on the island's north side and faces roughly north-northwest (Figure 1b). This makes it partially sheltered from trade wind conditions, but exposed to seasonally high episodic swell events between October and May. These swells are usually generated from remote sources to the north and west (NW), with 1–5 m waves and 12–20 s periods common during these months; wave heights in excess of 6 m may occur several times a year. During these swell events, winds typically slacken or become westerly and rotate clockwise back to the northeast, as cyclonic low-pressure systems producing the swell pass to the north, although this is not always the case. Tropical and extratropical cyclones (the latter known as 'Kona' storms) also occasionally impact the island; however, these mostly affect the south and west sides of the island.

[7] Fringing reef platforms are found on the east and west sides of the bay; the western reef (Queen's Reef) generally has a more gradual reef slope (~6–12°) and deeper reef flat (~1–4 m), while the eastern side (Hanalei Reef) is somewhat steeper (reef slope of 10° to nearly vertical) and has an extensive area of reef flat less than 1 m deep. A detached deeper reef (King's Reef) lies approximately 1 km offshore and has a minimum depth of ~16 m. This offshore reef affects incident gravity wave refraction patterns and has been known to break when waves exceed 5 m. These reefs are composed primarily of coralline alga, with live coral cover ranging between 2% and 47%, with an average of about 18% [*Friedlander and Brown*, 2005]. Most other areas in the bay tend to be made up of flat or gently sloping sand or gravel [*Calhoun et al.*, 2002].

[8] The Hanalei watershed is one of the three priority watersheds in Hawaii identified for focused action to address land-based pollution threats to coral reefs by the U.S. Coral Reef Task Force. These and other environmental concerns have prompted a number of studies in the area [e.g., *Friedlander and Parrish*, 1997; *Calhoun et al.*, 2002; *Friedlander and Brown*, 2005] (more recent studies are summarized by *Field et al.* [2007]).

2.2. Determination of Wave Climate

[9] The National Oceanographic and Atmospheric Administration's (NOAA) National Data Buoy Center (NDBC) Buoy 51001, 314 km northwest of Kauai in 3430 m of water (Figure 1a), provides measurements of directional wave parameters, wind speed and direction, sea level barometric pressure, and sea surface water and air temperature (http://www.ndbc.noaa.gov). This buoy will be referred to as Buoy 51001 for the remainder of the document. While it is located some distance from the study site (~300 km), the buoy measurements can be considered representative of trade wind wave and NW swell contributions to wave climate immediately offshore from the study site (modeling results presented here suggest this to be the case). Wave height climatologies were constructed by calculating means, standard deviation, and minimum and maximum for each month for all available observations of significant wave height (H_s) between 1981 and 2009. Directional wave climatologies were constructed by discretizing all available bulk wave parameters of H_s into 2 s peak period (T_p) by 5° peak wave direction (θ_p) bins between years 2005 and 2009. These binned values were then analyzed for (1) mean bin event frequency of occurrence and (2) mean significant wave height for each bin. This allows for an examination of how often (in a year or season) a particular wave direction/frequency event tends to occur and its average magnitude (height). The maximum entropy method [*Lygre and Krogstad*, 1986] was used to calculate directional wave energy spectra ($E_{(\sigma,\theta)}$) from Buoy 51001 pitch and roll data. Conditions were classified as "trade wind" or "NW swell" when wave energy (E), defined as

$$E = \int_{\sigma=j}^{\sigma=k} \int_{\theta=m}^{\theta=n} E_{(\sigma,\theta)} d\sigma d\theta, \tag{1}$$

integrated over frequency (σ) and directional (θ) sectors fell into a range of values associated with the respective conditions, as defined by the directional climatologies (see results for definition of these σ, θ, and E values). Additionally, the Buoy 51001 directional spectra were used as input to the numerical wave models, as discussed below.

[10] Since the time period of available Buoy 51001 directional wave data was considered somewhat too short to effectively characterize directional wave climate (4 years), climatologies were also constructed from National Environmental Predictions Center (NCEP) Wave Watch III Version 2.22 NE Pacific Model (0.25° spatial resolution) output (referred to as WW3 for the remainder of the document, see http://polar.ncep.noaa.gov/waves and *Tolman* [2002] for an overview). WW3 bulk parameter hindcast data (H_s, T_p, and θ_p) are available from 1996 to 2009. The same methods used to compute Buoy 51001 directional climatologies were applied to WW3 hindcast data from the same location as Buoy 51001. Additionally WW3 hindcast bulk wave parameters, spectral data, and gridded wind fields were tested as input to a fine-scale coastal wave model, as discussed below.

2.3. Nearshore In Situ Data Collection

[11] Physical measurements inside the bay were recorded at four bottom-mounted acoustic Doppler current profiler

Table 1. Instruments Deployed in or Near Hanalei Bay for This Study[a]

Site	Instrument	Depth (m)	Dates
Wall	RD Instruments ADCP (600 kHz)	10.0	7 Jun 2006 to 24 Apr 2007
NW Reef	Sontek ADCP (1 MHz)	14.5	14 Sep 2006 to 24 Apr 2007
CRAMP	Nortek ADCP (1 MHz)	9.7	7 Jun 2006 to 7 Sep 2006
SE Reef	Nortek ADCP (1 MHz)	10.5	7 Jun 2006 to 7 Sep 2006

[a]Deployments depths and dates are given; for deployment locations, refer to Figure 1b.

(ADCP) mooring sites between 7 June 2006 and 7 April 2007. Details of these instrument platforms are given in Table 1 and their locations are plotted in Figures 1a and 1b. The Wall site, proximate to the near-vertical rise of Hanalei Reef from the seabed at around 10 m of a depth to approximately 2 m in this area, was located near the mouth of the Hanalei River. The SE Reef site, proximate to a small reef outcropping, was located near the center of the bay. The CRAMP site (colocated with a University of Hawai'i at Mānoa Coral Reef Assessment and Monitoring Program site [*Jokiel et al.*, 2004]) was located on the western side of the bay at the base of the Queen's Reef forereef; the NW Reef site is farther north along the base of Queen's Reef from the CRAMP site.

[12] Sampling strategies allowed for water velocity profile and mean sea surface (observed tide) to be measured at least every 30 min, and directional wave parameters at least once an hour during observation periods. A high-frequency cutoff 0.25 Hz (T = 4 s) seconds was used for the pressure (PUV) based wave calculations (Nortek and Sotek/YSI instruments) to remove potential measurement errors in the high-frequency part of the spectrum, i.e., the pressure response factor corrections [*Dean and Dalrymple*, 1991]. This cutoff is lower (more conservative) than that suggested by the instrument manufacturers, even at the deepest mooring (14.5 m). Neglecting these higher frequencies in waves calculations is not considered a significant source of error in this study, since measured wave energy in these higher frequencies at the Wall site, which used acoustic surface tracking to help characterize waves, was very low ($\ll$5% of total); also peak frequencies measured at Buoy 51001 (see description below) were <0.2 Hz 99.9% of the time between years 2005 and 2009. Harmonic analysis [*Pawlowicz et al.*, 2002] of pressure time series at the Wall and NW Reef sites (both) resulted in six astronomic tidal constituents (M2, S2, O1, K1, N2, and SK3) with signal-to-noise ratios greater than 10; these were used to predict tidal elevations during model runs.

2.4. Wave Model Implementation

[13] The SWAN model (version 40.72AB), a phase-averaged solution of the discrete spectral balance of wave action density [*Booij et al.*, 1999], was selected to estimate wavefields within the bay. This approach conserves action density (N), defined as wave energy (E) divided by relative frequency (σ). The propagation of N in time (t), space (x, y), and frequency and direction (σ, θ) is described by

$$\frac{\partial}{\partial t}N + \frac{\partial}{\partial x}c_x N + \frac{\partial}{\partial y}c_y N + \frac{\partial}{\partial \sigma}c_\sigma N + \frac{\partial}{\partial \theta}c_\theta N = \frac{S_{tot}}{\sigma}. \quad (2)$$

In the second and third terms, the velocities c_x and c_y are components of group speed; the third and fourth represent frequency shifting and refraction due to changes in current and depth, respectively; c_σ and c_θ describing the rates of change. The wavefield propagation (left side) is balanced by the source terms (S_{tot}) on the right; the source terms are composed of

$$S_{tot} = S_{in} + S_{wc} + S_{nl4} + S_{fr} + S_{br} + S_{nl3}. \quad (3)$$

These individual source terms are wind generation (S_{in}), dissipation (white capping S_{wc}, bottom friction S_{fr}, and breaking S_{br}), and nonlinear interactions (quadruplets S_{nl4} and triads S_{nl3}).

[14] Due to the predominance of relatively large, mature seas in the area and the small spatial scale of the local model, surface wind processes were not considered significant to the processes of interest, and S_{in} and S_{wc} were not included in the local model. In the larger-scale models, however, wind growth (S_{in}) and whitecapping (S_{wc}) were included. For more information on model formulations and validation of SWAN, see *Booij et al.* [1999] and *Ris et al.* [1999]; *Mulligan et al.* [2008a, 2008b] provide a succinct overview, including some new developments not included by *Booij et al.* [1999].

2.4.1. Local Model Simulations

[15] Two 1 week periods were selected for model development and validations: 2–9 August 2006 and 20–27 January 2007; the first characterized by trade wind conditions and the second NW swell. To estimate the wavefield within Hanalei Bay and immediately offshore during these two periods, a rectangular Cartesian coordinate grid was constructed (local grid); this grid extends 8 km on either side of the bay and 5 km offshore of the mouth of the bay (Figure 1a). Simulations were carried out on the grid at (Δx, Δy =) 200, 100, and 40 m spatial resolutions; a subdomain, extending 2.5 km either side of the bay and 3.0 km offshore, was nested within the 40 m spatial resolution grid and simulations carried out at 30, 20, and 10 m resolutions.

[16] Frequency space was resolved with 25 logarithmic bins from 0.04 to 0.40 Hz ($\Delta\sigma/\sigma$ = 0.1). Directional resolution was varied from $\Delta\theta$ = 5° to $\Delta\theta$ = 1°; implementations of refraction were tested; and simulations with and without phase-decoupled estimated diffraction [*Holthuijsen et al.*, 2003] were conducted.

[17] Model bathymetry was interpolated from two different sources: lidar data in shallower areas (provided by the U.S. Army Corps of Engineers, http://shoals.sam.usace.army.mil) and multibeam acoustics (provided by University of Hawai'i Benthic Habitat Mapping Center, http://www.soest.hawaii.edu/pibhmc) in deeper areas. In almost all cases, bathymetric data resolution was far higher than computation grid cell resolution; grid bathymetric errors due to interpolation in data poor areas are considered insignificant.

[18] The formulation of *Madsen et al.* [1988] was used to estimate bottom friction; wave hydraulic roughness length

(k_w) scales were varied from 0.01 to 0.20 m, the higher range of values (0.10–0.20 m) suggested for coral reefs [*Hearn*, 1999; *Lowe et al.*, 2005]. Simulations with both spatially fixed and varied roughness values were carried out, with higher values for reef substrate (~0.10–0.20 m) than for unconsolidated sediment (sand, ~0.01 m). Areas of reef and sand were differentiated through a combination of bathymetric slope analysis and visual inspection of aerial photography, IKONOS, and Quickbird satellite imagery. A value for the empirical breaker height coefficient ($\gamma_b = H_m/h$, where H_m is "maximum allowable wave height" and h is local water depth) was calculated using *Massel and Gourlay*'s [2000] equation 27 for reef slope dependent maximum allowable wave height (which they derive from *Singamsetti and Wind* [1980]). A mean slope of 0.1 (estimated as the slope of Hanalei's forereefs, estimated from bathymetry data) resulted in a value of 0.8 for γ_b used for all modeling runs. The wave breaking dissipation coefficient (α) was set to 1.0, a value used in similar modeling efforts [e.g., *Battjes and Janssen*, 1978; *Mulligan et al.*, 2008b]. An analysis of model sensitivity to these coefficients is presented by R. Hoeke et al. (manuscript in preparation, 2011). Water elevations predicted from the tidal constituents were varied uniformly over the model grid for all simulations.

2.4.2. Generation of Wave Boundary Conditions

[19] Unfortunately, the nearest measurements of deep-water waves available to drive the local wave model grid was a University of Hawai'i maintained directional wave rider buoy approximately 170 km away off the north coast of the island of Oahu. This buoy was not considered for input, as it is largely sheltered from typical trade wind waves by Oahu and may be partially sheltered by Kauai during NW swell events. As significant evolution of the wavefield may occur in the intervening 300 km between the local grid and the other nearest deepwater wave measuring device, Buoy 51001, an alternate source of wave forcing of the local grid was required.

[20] Generation of input wave forcing was initially attempted by applying bulk wave parameters (H_s, T_p, θ_p) provided by WW3, and an estimated directional spreading (s_p) at the local model's offshore grid boundary. This was quickly abandoned, as it neglected multiple peaks in the real spectrum (often present in the Hawaiian Archipelago) and likely was generally a poor representation of real directional frequency energy spectra under most conditions. This led to the evaluation of two directional spectral input methods, one based on WW3 and the other based on Buoy 51001 data, necessitating the construction of two coarse resolution SWAN grids (Figure 1a).

[21] The first grid was a 1 km spatial resolution curvilinear grid nested within WW3 spectral output nodes surrounding the island of Kauai (WW3 input model, Figure 1a); the second, a 2 km resolution orthogonal grid with the northwest corner at the location of Buoy 51001 and the southeast corner at the eastern midpoint of the island of Kauai (Buoy 51001 input model, Figure 1a). Forcing for the WW3 input model came from the WW3 nodes and gridded wind fields; for the Buoy 51001 input model, Buoy 51001 directional spectra were applied at all boundaries, and Buoy 51001 measured winds applied uniformly over the domain. Directional spectra from these two input models were saved at points along the offshore local grid domain. These spectra (from both input models) were separately interpolated along the local grid's offshore boundaries to provide two sources of (local grid boundary) input.

2.4.3. Validation of Local Model Simulations

[22] The effect of differing boundary conditions (from the two input models above) and local model parameterizations on the prediction quality of the nearshore wavefield was evaluated through examination of bias error, root-mean-square error (RMSE) and normalized model skill or "error performance" scores associated with each model run. These metrics were calculated from differences in the corresponding sets of (model) predictions and (in situ) observations of H_s, T_p, and θ_p at available grid points. Measurement errors in observations were assumed to be trivial in comparison to model prediction errors [*Willmott et al.*, 1985]. Bias error was used in addition to RMSE as it retains its sign (at individual locations), providing useful additional information on variable error linkages (e.g., showing underestimation of H_s linked to θ_p bias through underestimation of refraction). The primary model skill scores used for evaluation (and presented in section 3) are as follows:

$$\text{RMSE skill} = 1 - \frac{\left\langle (predictions - observations)^2 \right\rangle^{1/2}}{\left\langle (observations)^2 \right\rangle^{1/2}}, \quad (4)$$

$$\text{bias skill} = 1 - \frac{\langle |predictions - observations| \rangle}{\left\langle (observations)^2 \right\rangle^{1/2}}, \quad (5)$$

$$\text{angular bias skill} = 1 - \tan^{-1}\left[\frac{\sum \sin(predictions - observations)}{\sum \cos(predictions - observations)}\right] \cdot \frac{1}{180}. \quad (6)$$

The symbols $\langle\ \rangle$ denote the mean of the enclosed values. The values for prediction and observation used in angular bias skill are θ_p in degrees. These quantities are discussed by *Hanson et al.* [2006] and are similar to model performance evaluation metrics used by *Mulligan et al.* [2008a], *Ris et al.* [1999], *Sutherland et al.* [2004], and *Willmott et al.* [1985].

3. Results

3.1. Wave Climate

[23] The monthly H_s climatology illustrates the highly seasonal nature of the region's wave climate (Figure 2). In the summer H_s generally averages 2 m ± 0.5 m; while mean wintertime H_s is only about 1 m higher, the range of observed heights is far greater, with mean monthly maximum wave heights in the range of 6–7 m during December, January, and February. This relatively low range in wave heights during the summer is due to the ubiquitous dominance of trade wind waves ($H_s \sim$ 1–3 m, $T_p \sim$ 6–8 s, $\theta_p \sim$ 60–115°), illustrated by the directional wave climatologies (Figure 3). While trade wind waves may also frequently occur in winter months, episodes of northwest swells, ($H_s \sim$ 2.5–3.5 m, $T_p \sim$ 12–16 s, $\theta_p \sim$ 300–330°) occur, on average, about 90 days each year.

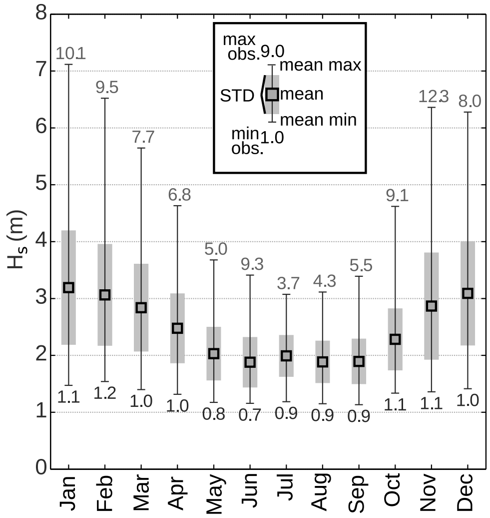

Figure 2. Climatological monthly mean, standard deviation, and mean monthly minimum/maximum and total observed minimum/maximum significant wave height at Buoy 51001 for years 1981–2009.

More extreme events ($H_s > 4$ m, $T_p \sim 16$–20 s, $\theta_p \sim 300$–$330°$) also occur with measurable regularity (~10 times in an average season [*Vitousek and Fletcher*, 2008]), although much less frequently than the smaller, slightly shorter-period NW swells (Figure 3).

[24] Recent Buoy 51001 directional data are of much more limited temporal extent (3 years) than WW3 (11 years) and coincides roughly with the timing of this study. Although they are in good agreement, the Buoy 51001 statistics show a greater occurrence of trade wind conditions in the winter and a slightly more northerly direction in most occurrences of NW swells. These subtle differences over the last few years from longer term means may be linked to inter- and intradecadal climate oscillations [e.g., *Rooney and Fletcher*, 2005] or may be an expression of model bias, especially for the mature NW swell events [*Hanson et al.*, 2006]. Further investigation of differences between short-term (3 years) in situ derived and longer-term (11 year) model derived wave climatologies is beyond the scope of the work presented here.

[25] The wave climatologies discussed above were used to classify conditions during the study period. Trade wind conditions were defined as E between 0.6 kJ/m^2 and 5.625 kJ/m^2 for $\sigma \geq 0.083$ Hz, θ between 45 and 135° sector (this corresponds to $H_s \sim 1$–3 m, $T < 2$ s), as measured in Buoy 51001 spectra. NW swell conditions were defined as $E > 2.5$ kJ/m^2 in the $\sigma \leq 0.1$ Hz, θ between 295 and 360° sector (this corresponds to $H_s \geq 2$ m, $T > 10$ s). These two classifications were not necessarily mutually independent, as simultaneous peaks in both areas of the directional spectrum often occurred, i.e., often both criteria were fulfilled during periods of when NW swells and trade wind conditions simultaneously occurred. Figure 4 plots in situ measurements during the study period and highlights times falling within one or both of the classifications; trade wind conditions were experienced 77% of the total time, while NW swells occurred 9% of the time. Both trade wind conditions and episodic NW swell conditions occurred 4% of the total time or 49% of the time during the swell events. Periods that fell outside of the two classifications were generally quiescent, both in terms of wave energy and winds.

3.2. Nearshore In Situ Observations

[26] While trade wind waves reached height in excess of 3 m offshore several times during the study period, they never resulted in measured waves greater than 2 m, and were usually much less, inside the bay (Figure 4a). NW swell events, on the other hand, frequently resulted in measured wave heights in excess of 3 m, and at times in excess of 5 m, inside the bay (Figure 4a). Fundamental differences in both overall current magnitudes and circulation patterns within the bay under the two different conditions are also evident; with only two exceptions during the study period, currents measured at the Wall site remain below 0.20 m/s, usually on the order of 0.05 m/s, during trade wind conditions; during NW swell events, currents in excess of 0.50 m/s frequently occur (Figure 4d and Table 2).

[27] Table 2 summarizes statistical differences between the two conditions as observed at the in situ monitoring sites. Significant correlations between wave heights and current magnitudes occur at all sites within the bay occur during NW swell events (r = 0.55–0.80), correlations with wind stress magnitude and (predicted) tidal elevations are low (<0.15) or insignificant. Conversely, only the Wall site shows correlation between waves and currents throughout the water column during trade wind conditions (r = 0.43–0.53); other sites show higher correlation with tides and wind. Tide appears to contribute to the low currents magnitudes lower in the water column (r = 0.42–0.54), while winds appear to contribute to forcing in the upper water column at the CRAMP and SE Reef sites (r = 0.42–0.46) and wind. Low modal river discharge (<20 m^3/s over 95% from a stream gauge record of Hanalei River) and low vertical and horizontal density gradients (generally $\Delta\rho \ll 1$ kg/m^3) in observed conductivity, temperature and depth (CTD) profiles within the bay [*Storlazzi et al.*, 2006, 2008; *National Marine Fisheries Service*, 2006] suggest buoyancy forcing contributes little to overall flow regime during most conditions and thus is not included at a forcing variable in Table 2. While buoyancy forcing may become important during large freshwater discharges associated with occasional floods of the Hanalei River, due to their rarity [*Draut et al.*, 2009] and the lack of observations of resulting salinity/density gradients, buoyancy forcing is not considered further in this paper.

[28] Differences in circulation patterns are further visualized though examination of the principle axes and Eularian mean currents under the two different wave conditions (Figure 5). During trade wind conditions, consistent with the weak but significant correlation of near-bottom currents with tidal elevations in Table 2, near bottom principal axes are poorly defined but roughly aligned with bottom contours and show little asymmetry at all locations; near surface means are roughly a factor of 2 stronger and tend to show significant net directions (asymmetry). On the western side of the bay, mean vectors are roughly aligned with the direction of the trade winds, suggesting onshore wind driven

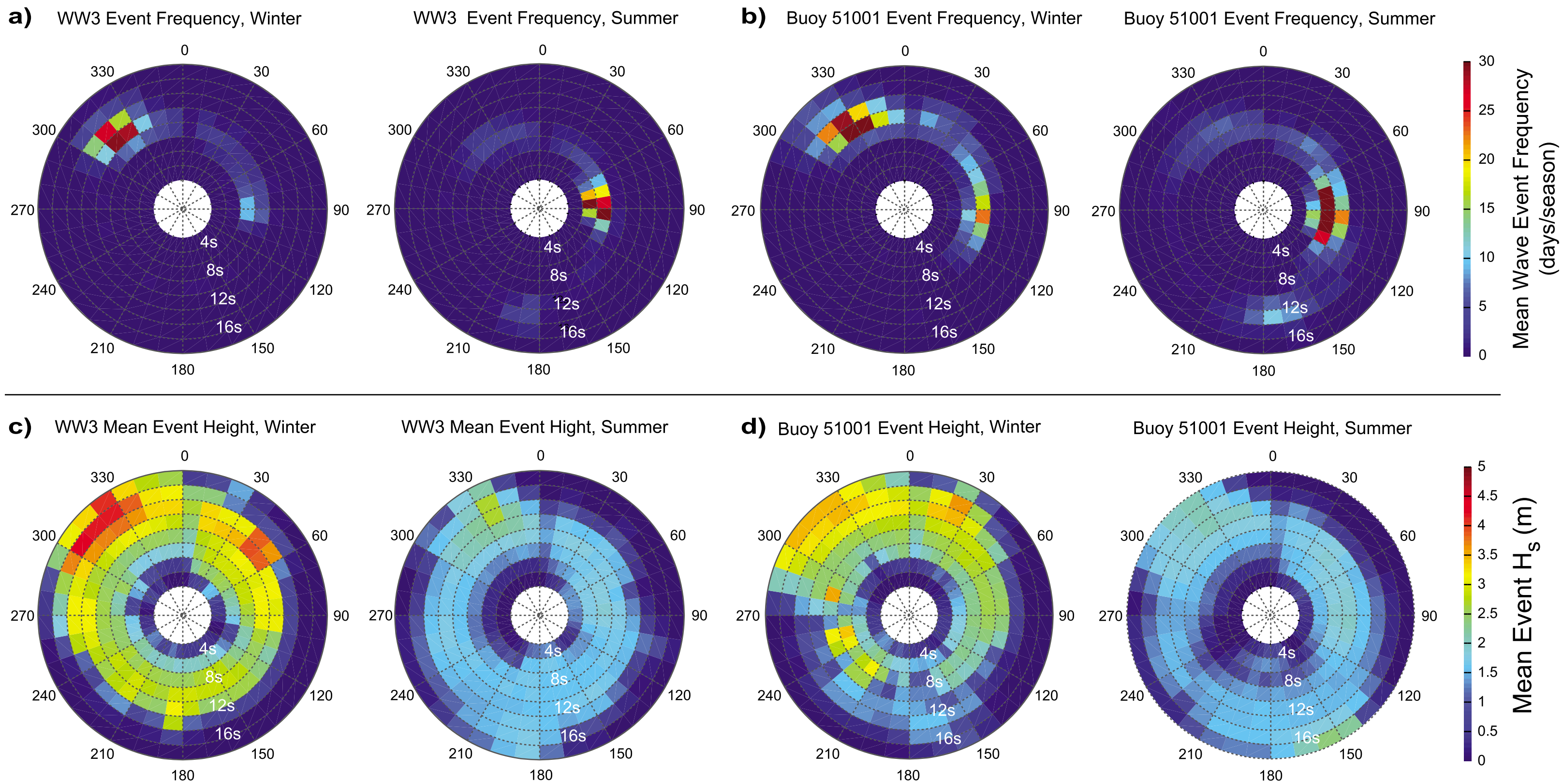

Figure 3. Seasonal directional wave climatologies generated from model hindcast data from 1996 to 2009 (WW3) and in situ buoy data from 2005 to 2009 (Buoy 51001). (a) WW3 mean event frequency for November–March (winter) and May–September (summer). (b) Buoy 51001 mean event frequency for winter and summer. Mean event frequency is defined as the occurrence of peak direction (θ_p) and peak period (T_p) in each directional/period bin in the historical data, normalized to represent mean number of days occurrence in each season; e.g., if the color indicates 30, then on average the condition occurs on 30 out of 150 days each season. Scaling for both Figures 3a and 3b is given by the colorbar to the right. (c) WW3 mean significant wave height for all observations in each θ_p, T_p bin for summer and winter. (d) Buoy 51001 mean significant wave height for summer and winter. Events occurring during the months of April and October, transition months, are omitted from the analysis for clarity.

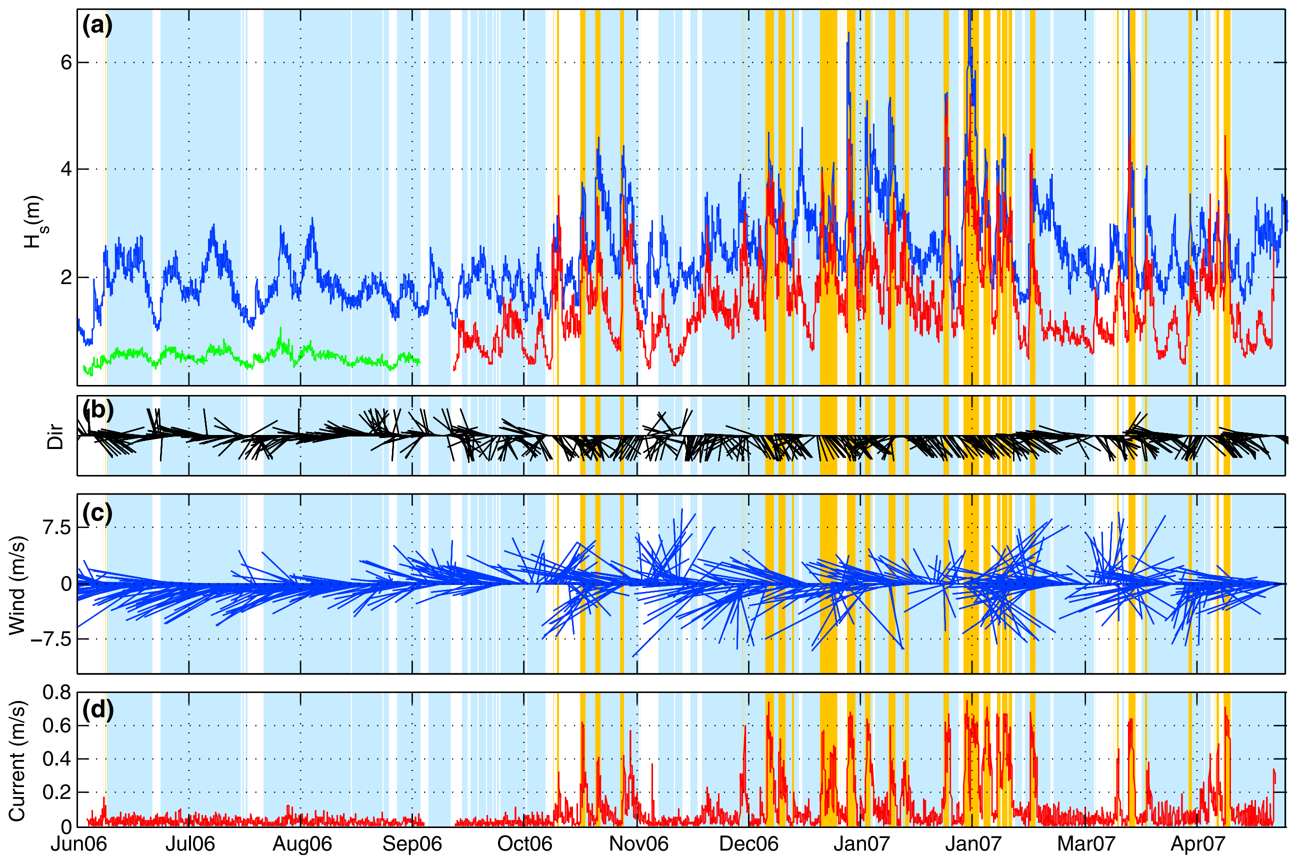

Figure 4. In situ waves, winds, and currents during the study (5 June 2006 to 10 April 2007). (a) Significant wave heights at Buoy 51001 (blue), CRAMP (green), and NW Reef (red) sites. (b) Daily mean wave direction at Buoy 51001 CCW from true north. (c) Daily mean wind vector at Buoy 51001. (d) Current magnitude at the Wall site. Trade wind conditions are identified with light blue bands, episodic NW swell conditions are indentified with yellow bands; note the two conditions are not mutually exclusive. Conditions not classified as trade wind or NW swell (white areas) are generally quiescent. See the text for parameterization of the conditions.

flow, while the mean vectors are oriented toward the shoreline on the eastern side of the bay (Wall site), suggesting wave driven flow, also supported the higher correlation of currents and waves at this site (Table 2). During NW swell events, currents at the Wall site are strongly oriented into the bay along the principle axis throughout the water column. Observations on the western side of the bay suggest that this flow tends to exit the western mouth of the bay, visible in the orientation of the principle axes at the NW Reef and CRAMP sites (Figure 5).

Table 2. Mean and Standard Deviation of Observed Significant Wave Height H_s and Current Magnitude $|U|$ at Instrument Sites During Trade Wind Conditions and During NW Swell Episodes[a]

	Trade Wind Conditions					NW Swell				
	H_s (m)	$\|U\|$ (m/s)	R_{tide}	R_{wind}	R_{wave}	H_s (m)	$\|U\|$ (m/s)	R_{tide}	R_{wind}	R_{wave}
Wall	0.24(0.07)	0.05(0.07)	**0.21**	0.10	**0.53**	0.47(0.15)	0.37(0.21)	−0.01	−0.05	**0.64**
		0.03(0.04)	**0.54**	0.07	**0.43**		0.22(0.14)	−0.08	0.03	**0.71**
NW Reef	1.30(0.59)	0.09(0.05)	**0.29**	**0.41**	**0.46**	2.57(0.89)	0.21(0.13)	**0.12**	−0.08	**0.69**
		0.04(0.02)	**0.42**	0.05	**0.17**		0.09(0.07)	**0.15**	**0.13**	**0.63**
CRAMP	0.54(0.10)	0.14(0.10)	**0.39**	**0.46**	**0.24**		0.17(0.14)	0.68		**0.77**
		0.01(0.01)	**0.44**	**0.26**	**0.10**		0.02(0.01)	0.34		**0.28**
SE Reef		0.06(0.04)	**0.26**	**0.42**	**0.21**		0.06(0.03)	0.59		**0.80**
		0.02(0.01)	**0.46**	−0.06	**0.06**		0.02(0.01)	0.32		**0.55**

[a]Standard deviation is given inside the parentheses, while mean is given outside the parentheses. Correlation between $|U|$ and predicted tide (R_{tide}), squared wind speed (R_{wind}), and H_s at the most exposed ADCP site (R_{wave}) are given; significant correlation values ($p < 0.01$) are indicated in bold. The first row of values is derived from near-bed ADCP bins (lowest approximate 1.5 m of the water column), and the second row of values is derived from with the near-surface ADCP bins (uppermost approximate 2 m of the water column). No values indicate insufficient data.

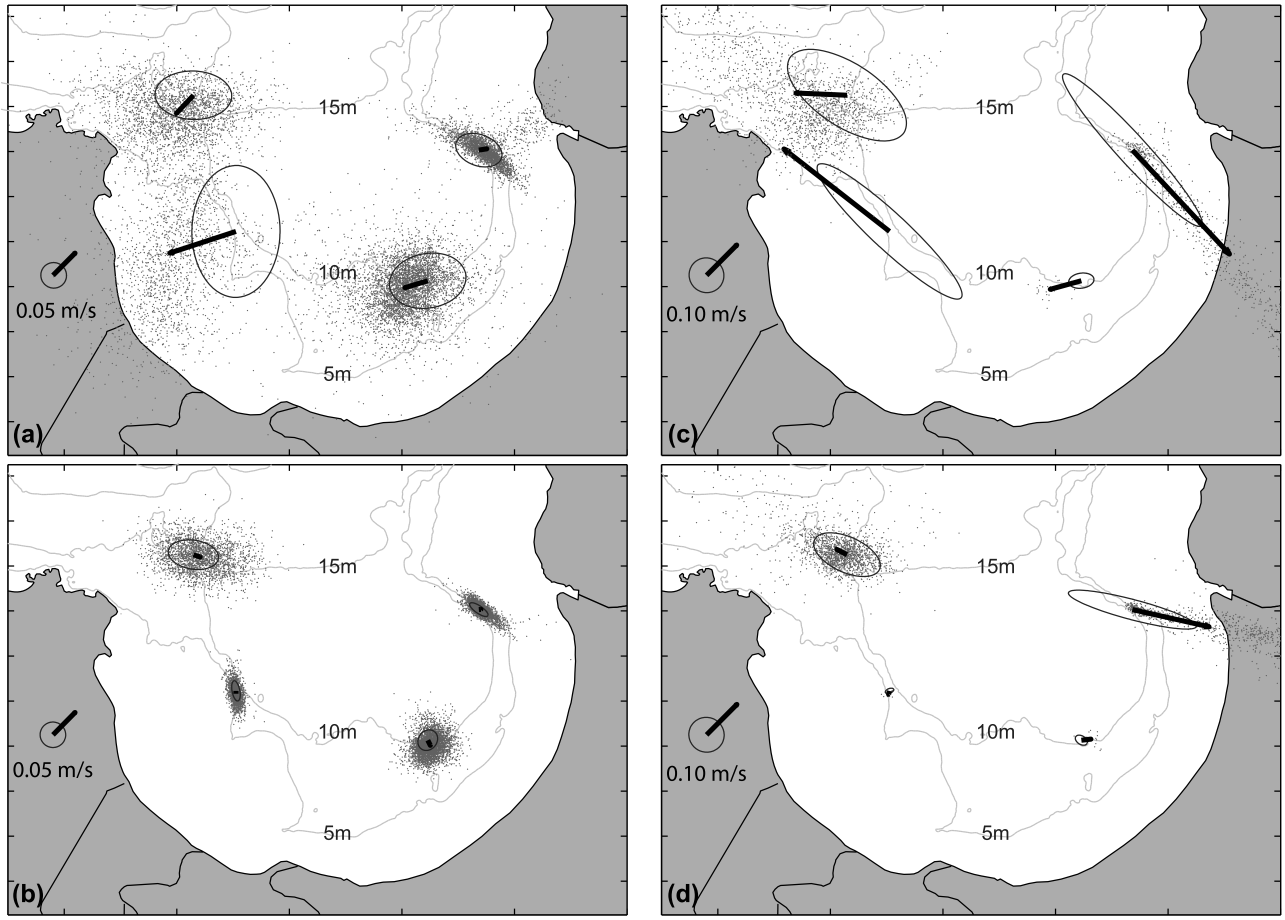

Figure 5. Variance ellipses and Eularian mean vectors of in situ ADCP data plotted at their respective locations in Hanalei Bay: (a) near-surface bin during trade wind conditions, (b) near-bottom bin during trade wind conditions, (c) near-surface bin during episodic NW swell events, and (d) near-bottom bin during NW swell events. Individual observations are indicated by scatter points; scaling is given by arrows and ellipses on the left. Note differences in scaling: In Figures 5a and 5b, vector scale arrows correspond to 0.05 m/s and error ellipse scales correspond to a *u*/*v* standard deviation of 0.02 m/s; in Figures 5c and 5d, arrow and ellipse scales correspond to 0.1 and 0.04 m/s.

[29] The fact that the semimajor axis of flow is strongly oriented into the bay at the Wall site during NW swell events, and to a lesser extent during trade wind conditions, suggests that wave-driven flow over Hanalei reef is a significant circulation driver within the bay. Unfortunately, the bay's complex fringing reef topography and exceptionally high wave height at exposed locations during larger NW swell episodes (instrumentation typically will not survive) limit the availability of in situ observation locations. This has made the relationships between incident wave height (H_0), setup (η) and resulting residual flows ($\overline{u}$) difficult to elucidate compared to similar studies where instrumentation has been deployed in transects perpendicular to relatively linear reef slopes, crests, and flats [e.g., *Hearn*, 1999; *Gourlay and Colleter*, 2005; *Lowe et al.*, 2005, 2009; *Hench et al.*, 2008]. This difficulty is exacerbated by the nonlinear interaction of differing incident wave refraction patterns, tides, and wind.

[30] To simplify this comparison and draw generalizations on the effect of waves on flow in the bay, we focused on the semimajor axis of current magnitude at the Wall site, which shows the greatest dependence on wave conditions and small variance in the semiminor direction (Figure 5). It was hypothesized that a large part of the observed variance in current would be proportional to the available wave energy flux (power) in the vicinity of the offshore reef slope

$$\overline{u} \propto EC_g. \tag{7}$$

Unit power can be estimated using the definitions of energy (E) and group velocity (C_g) from linear wave theory [*Dean and Dalrymple*, 1991], where g is gravitational acceleration, ρ is density of seawater h is mean water depth, and k is the wave number

$$EC_g = \frac{1}{8}\rho g H_s^2 \cdot \frac{g}{\omega}\tanh(kh) \cdot \frac{1}{2}\left(1 + \frac{2kh}{\sinh kh}\right). \tag{8}$$

When the depth-averaged velocities along the semimajor current axis (defined by NW swell conditions, Figures 5c and 5d) for all conditions at the Wall site ($\overline{u}_p$) are plotted against EC_g calculated from wave parameters measured at the NW Reef site (assumed to be a representative H_0 immediately

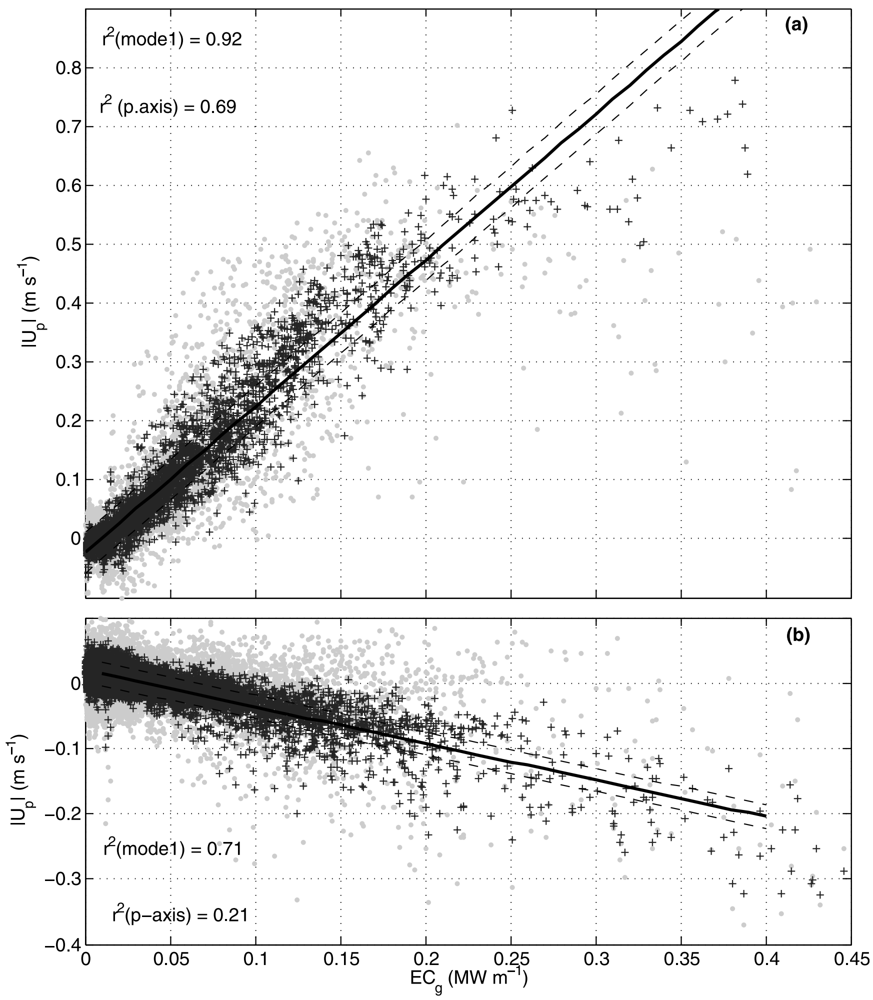

Figure 6. Depth-averaged current magnitude ($\overline{u}_p$) along semimajor axes at the (a) Wall and (b) NW Reef sites, both compared to wave energy flux values at the NW Reef site (EC_g). In Figures 6a and 6b, points correspond to unfiltered $\overline{u}_p/EC_g$ observations; crosses correspond to the first EOF mode of the data. Semimajor axes are defined by NW swell conditions at there respective sites, e.g., Figure 5c and 5d; positive values indicate flow along an axis oriented into the bay, and negative values indicate flow out of the bay. The solid and dotted lines are the (linear) regression line and the 50% error bounds, respectively.

offshore of Hanalei Reef), a significant linear relationship is evident (Figure 6a, r^2 = 0.69). The variability in this observed relationship can be further reduced by finding the first empirical orthogonal function (EOF) of the $\overline{u}_p/EC_g$ covariance matrix [*Emery and Thomson*, 2001]. This effectively filters out tides (band-pass filtering for tides was confounded, since swell events typically had frequencies on the order of 1 day), as well as other unknown forcing mechanisms. The first EOF mode described 92% of the observed variance of the data (Figure 6a), indicating that wave-driven flow dominates overall flow at the Wall site, even when available EC_g in the bay is small, typically during trade wind conditions.

[31] A similar, though less significant, relationship can be found for the (depth-averaged) current velocities ($\overline{u}_p$ oriented along the semimajor axis during NW swell conditions) and EC_g can be observed at the NW Reef site (1st mode EOF r^2 = 0.71, Figure 6b). This axis is primarily oriented out of the bay (Figures 5c and 5d). This further confirms that (wave energy dependent) flow over the bay's bordering reefs exits out the wide mouth of the bay, while the lower dependence suggest that this flow is less constrained by topography and more variable than that observed at the Wall site.

[32] If $\overline{u}_p$ at the Wall site, linearly related to incident EC_g (Figure 6a), is assumed to be representative of water flow over the morphologic feature of the "Wall," then the integration of $\overline{u}_p$ along this ~450 m long, ~2 m deep feature suggests volume fluxes on the order of 150 and 400 m^3/s for H_0 = 2 m and H_0 = 3, respectively. Calculating the volume of the bay inshore of the headlands as 1.90×10^7 m^3 below mean water level, flushing (residence) times for the bay are estimated to be on the order of 40 and 15 h from the above respective fluxes. The actual flushing times are likely less, since wave-driven flows over other reefs in the bay likely also contribute to the overall flushing. The importance of the contribution of wave action on this one reef to mean flushing of the bay is highlighted when compared to a simple, classical tidal prism flushing estimation [*Luketina*,

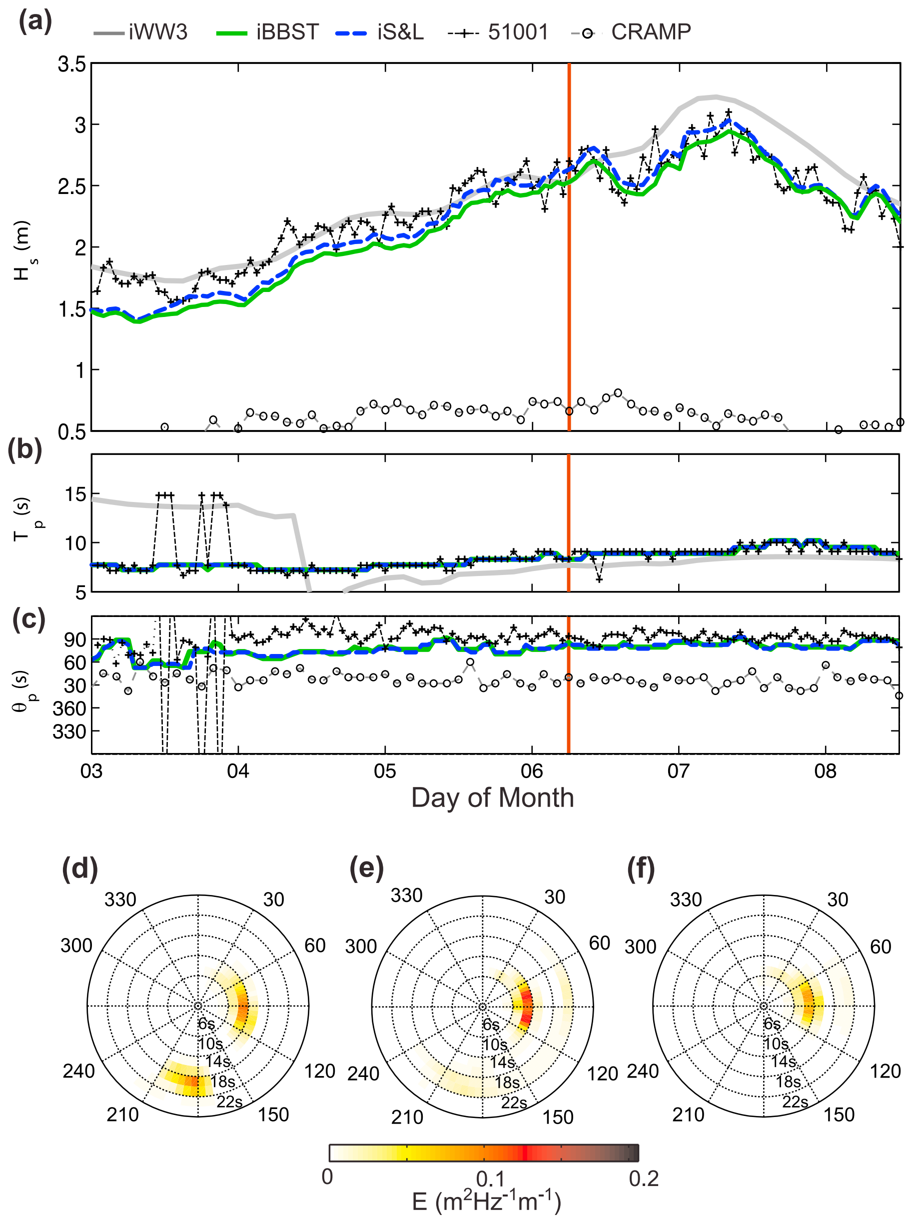

Figure 7. In situ wave observations and input model data for the trade wind conditions (2–9 August 2006): (a) significant wave height (H_s), (b) peak period (T_p), and (c) peak direction (θ_p). Here "iWW3" is the results of the WW3 input model at the center the local model offshore boundary, "iBBST" is the results of the Buoy 51001 input model using BSBT, and "iS&L" is the results of the Buoy 51001 input model using S&L (see text for description of these terms). Buoy 51001 and CRAMP in situ data are plotted for comparison; the vertical red line indicates time of accompanying spectra. (d) WW3 input spectra, NW corner; (e) Buoy 51001 input spectra; and (f) local model input from Buoy 51001 input model. The time series plot and the three spectra indicate the close correspondence of the WW3 and Buoy 51001 input with each other as well as the resulting modeled conditions at the offshore boundary. A long-period Southern Hemisphere swell is visible in Figures 7d and 7e; this is shadowed by the island of Kauai and thus non-existent in Figure 7f.

1998]. Defining the tidal prism as the volume difference between mean ebb and flood tidal levels suggests tidal flushing is on the order of 150 h.

3.3. Wave Model Simulations

[33] The conditions during the two 1 week periods selected for simulation of the nearshore wavefield, 2–9 August 2006 and 20–27 January 2007, were categorical of the trade wind and NW swell classifications, respectively. Wave conditions during the trade wind period gradually varying H_s of 1.5–3.0 m, T_p of 7.5–10.0 s, and θ_p of 80–100° at Buoy 51001 (Figure 7). Some long-period south swell ($T \sim 15.0$ s) occurred during the week, but as the area immediately offshore of the study site is completely sheltered from this

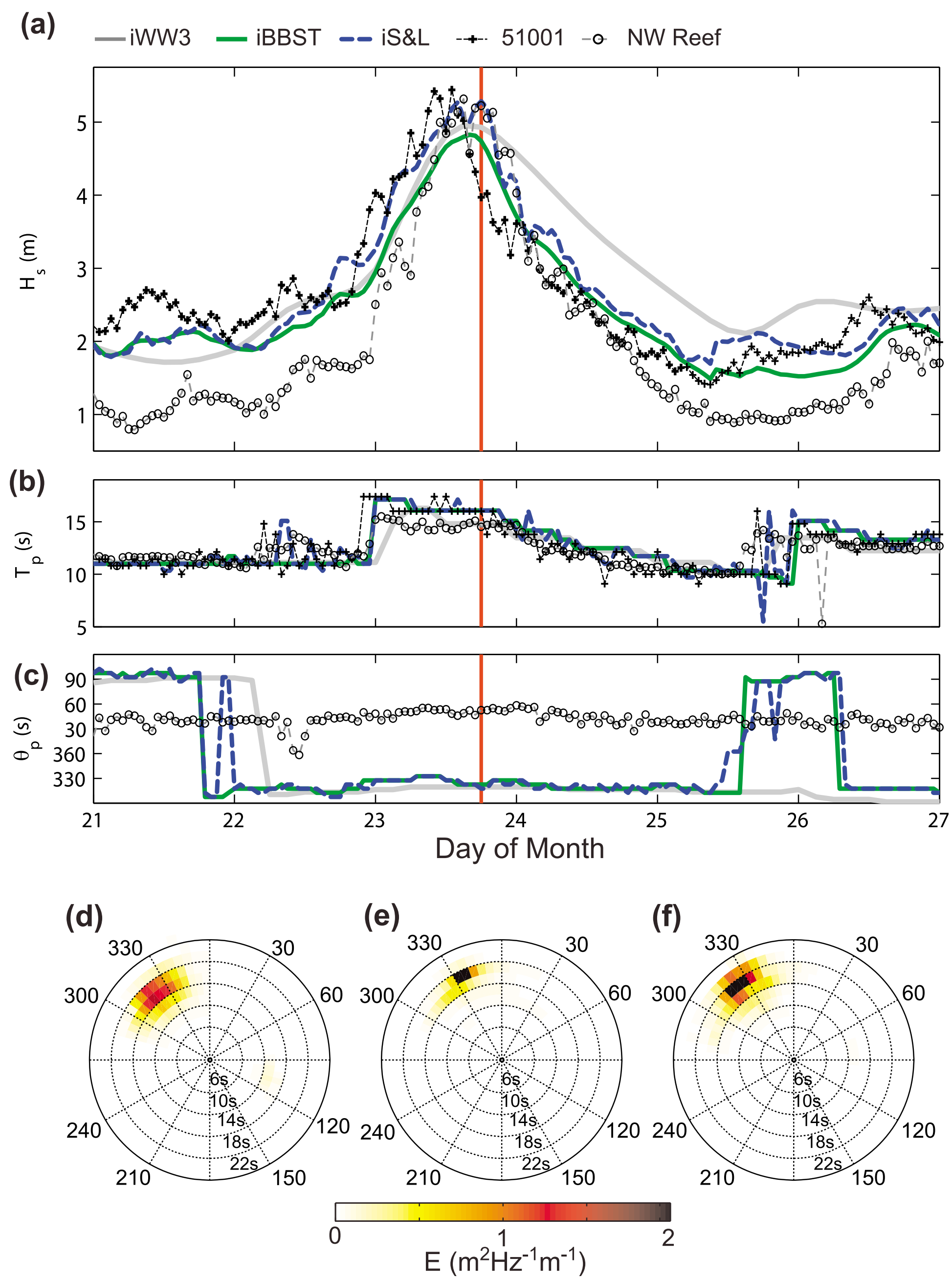

Figure 8. In situ wave observations and input model data for the NW swell event (20–27 January 2006): (a) significant wave height (H_s), (b) peak period (T_p), and (c) peak direction (θ_p). Here iWW3 is the results of the WW3 input model at the center the local model offshore boundary, iBBST is the results of the Buoy 51001 input model using BSBT, and iS&L is the results of the Buoy 51001 input model using S&L (see text for description of these terms). Buoy 51001 and NW Reef in situ data are plotted for comparison; the vertical red line indicates time of accompanying spectra. (d) WW3 input spectra, NW corner; (e) Buoy 51001 input spectra; and (f) local model input from Buoy 51001 input model. The time series plot indicate differences between WW3 and Buoy 51001 input and the resulting boundary conditions at the local model; use of either BSBT propagations or WW3 input tends to underestimate H_s relative to observed in situ H_s at the model boundary. The WW3 spectra is visibly more diffuse than that of Buoy 51001 near the peak of the swell (Figure 8d versus Figure 8e); Buoy 51001 input spectra leads to focused spectral energy at the local model boundary (Figure 8f).

Table 3. RMSE, Bias, and Skill of Significant Wave *Hs* and Normalized Skill of Peak Wave Direction θ_p for Selected Model Runs[a]

Run	Δx, Δy (m)	$\Delta\theta$ (deg)	k_w (m)	H_s RMSE (m)	H_s Bias (m)	H_s Skill	θ_p Skill
			Trade Wind				
1[b]	10	360	sand = 0.01, reef = 0.1	0.111	0.113	0.727	0.938
2[b]	10	120	sand = 0.01, reef = 0.1	0.113	0.117	0.725	0.935
3	10	120	sand = 0.01, reef = 0.1	0.118	0.105	0.689	0.929
4	40	120	sand = 0.01, reef = 0.1	0.129	0.122	0.658	0.936
5	40	120	uniform = 0.1	0.138	0.130	0.637	0.933
6	100	120	sand = 0.01, reef = 0.1	0.160	0.134	0.546	0.962
7	40	120	uniform = 0.01	0.161	0.154	0.554	0.982
8[c]	40	120	sand = 0.01, reef = 0.1	0.188	0.094	0.520	0.948
9	200	120	sand = 0.01, reef = 0.1	0.204	0.130	0.346	0.868
			NW Swell				
1	10	360	sand = 0.01, reef = 0.1	0.293	−0.181	0.800	0.885
2	10	120	sand = 0.01, reef = 0.1	0.300	−0.197	0.799	0.873
3	40	120	sand = 0.01, reef = 0.1	0.363	−0.339	0.780	0.932
4	40	120	uniform = 0.01	0.366	−0.327	0.757	0.877
5	40	120	uniform = 0.1	0.378	−0.350	0.752	0.874
6[c]	40	120	sand = 0.01, reef = 0.1	0.508	−0.412	0.528	0.865
7	100	120	sand = 0.01, reef = 0.1	0.750	−0.591	0.189	0.878
8	200	120	sand = 0.01, reef = 0.1	0.789	−0.513	0.018	0.793
9	100	72	sand = 0.01, reef = 0.1	0.844	−0.662	0.073	0.861

[a]Model run spatial resolution (Δx, Δy), directional spectral resolution ($\Delta\theta$), and hydraulic roughness (k_w) of each run are given. The listed H_s RMSE, H_s skill, and θ_p skill values are the averages for all observation sites for each entire model run. H_s bias values are only for the most exposed (NW Reef or CRAMP) set of observations.

[b]The inclusion of phase-decoupled diffraction is included in model solution. All model runs listed used the stationary second-order propagation scheme.

[c]Boundary conditions come from the third-order (S&L) propagation WW3 input model (all other listed runs use the S&L Buoy 1 input model).

direction, it is not considered relevant to the study. Buoy 51001 measured consistent trade winds during this period (~6–12 m/s from 60 to 90°). Maximum wave heights recorded in the bay during this period were H_s = 0.8 m and H_s = 0.4 m at the CRAMP and Wall sites, respectively. By contrast, the NW swell period saw a large, but not unusual, NW swell event; starting on 23 January, trade wind conditions rapidly gave way to increasing NW swell. At the swell's peak, Buoy 51001 measured H_s = 5.5 m, T_p = 17.5 s, and θ_p = 330° before subsiding back to trade wind conditions by 26 January (Figure 8). Buoy 51001 winds during the period were measured between 0 and 9 m/s, and winds rotated clockwise from the southwest to east, with northerly winds around 9 m/s preceding the peak of the swell by about 12 h. Maximum wave heights recorded in the bay were H_s = 5.3 and 0.9 m at the NW Reef and Wall sites, respectively.

[34] Efforts to minimize differences between observed and modeled wave conditions in the bay resulted in a large number of input model simulations (~40) and local model simulations (~80). The WW3 input model generally showed excellent agreement with the Buoy 51001 input model during the trade wind condition (Figure 7 and Table 3). During the January NW swell event, however, offshore WW3 input model energy was distributed over a broader range of frequencies and directions compared to the focused wave energy produced by Buoy 51001 input model. This more diffuse WW3 input generally resulted in smaller H_s within the bay compared to the Buoy 51001 input model (Figure 8) and poorer model skill (Table 3). This implies that the Buoy 51001 input model produced more realistic boundary conditions, especially during large mature swell events. As noted previously, inaccuracies in WW3 hindcasts during large mature North Pacific swells have been reported [*Hanson et al.*, 2006].

[35] The input models were sensitive to the numerical propagation formulation. First-order propagation schemes (e.g., backward space, backward time (BSBT)) proved far too diffusive in the input models, leading to output that smoothed over stochastic patterns common between Buoy 51001 and in situ observations within the bay during NW swell conditions. The third-order Stelling/Leendertse (S&L) [*Rogers et al.*, 2002] scheme proved far more satisfactory (Figures 7 and 8) for the input models. While the local model,

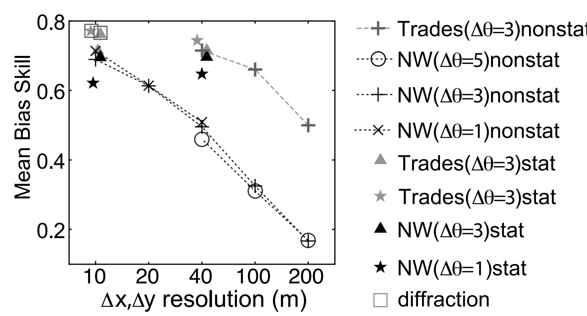

Figure 9. Comparison of overall composite mean bias skill scores for selected local model runs utilizing third-order (S&L) propagation Buoy 51001 input. Spatial (Δx, Δy) resolution of each run is given on the *x* axis. The legend indicates modeled condition (trades and NW for NW swell) and salient model parameterizations: directional spectral resolution in degrees (e.g., $\Delta\theta$ = 3) and propagation as "nonstat" for nonstationary first-order and "stat" for stationary second-order. The overall composite score is calculated by averaging all bias skill scores for H_s and θ_p at all in situ instrument locations; T_p is not included in the composite score since low variability in wave periods diluted (increased) poorer skill values.

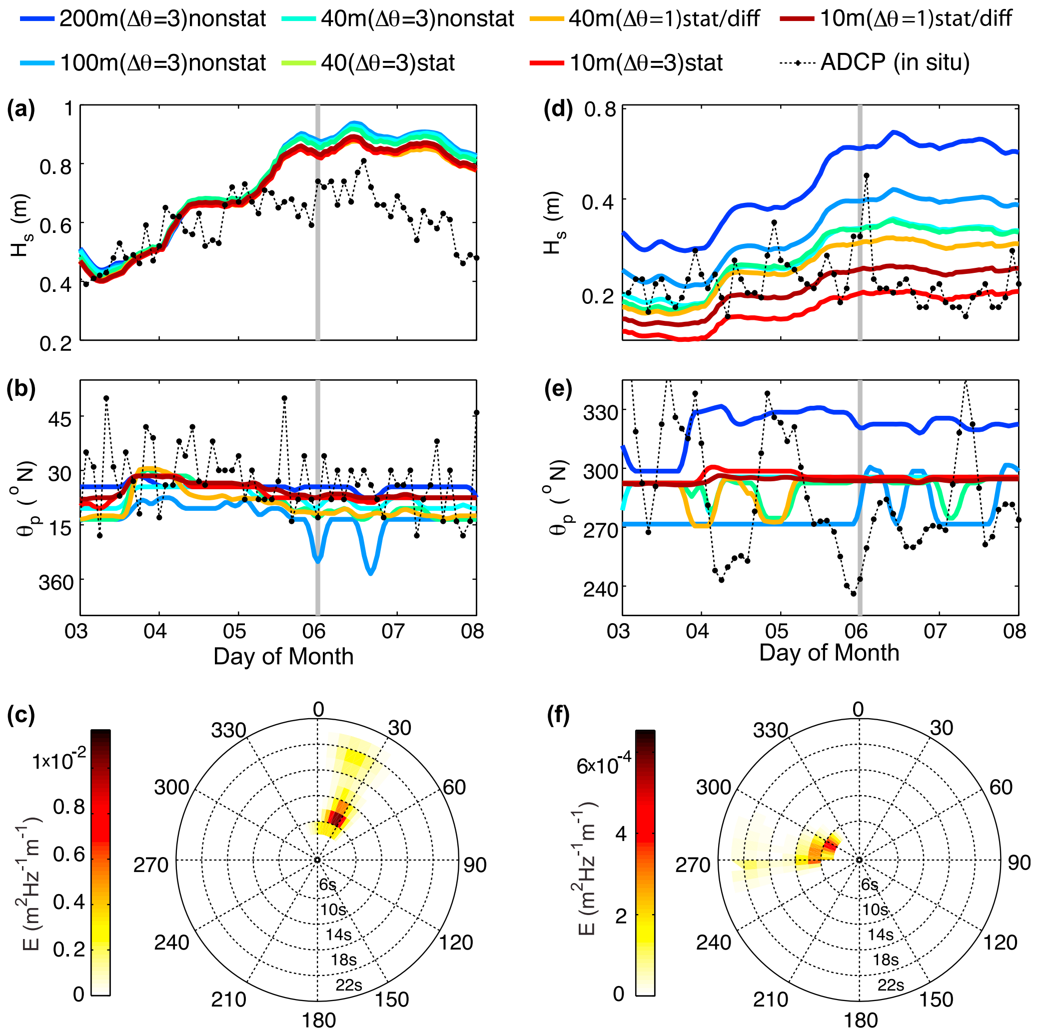

Figure 10. Comparison of varying model simulation resolution and propagation with in situ data during trade wind conditions, 2–9 August 2006. In the legend, the spatial resolution is given (e.g., 200 m) and the directional resolution in degrees (e.g., $\Delta\theta$ = 3) and propagation as nonstat for nonstationary first-order and stat for stationary second-order are defined; if diffraction is included, "diff" is added. (a) H_s at the CRAMP site. (b) Peak direction (θ_p) at the CRAMP site. (c) CRAMP model spectrum for the highest-resolution run (10 m($\Delta\theta$ = 3)stat/diff). (d) H_s at the Wall site. (e) Peak direction (θ_p) at the Wall site. (f) Wall model spectrum for the highest-resolution simulation (10 m($\Delta\theta$ = 1)stat/diff). The time of the spectra are indicated with a gray bar in the time series plots.

with its far smaller domain, did not appear to be as sensitive to propogation formulation, a second-order upwind (SORDUP) [*Rogers et al.*, 2002] scheme in quasi-stationary (stationary computations in nonstationary mode) generally appeared to optimize performance (Figures 9, 10, and 11). All model results discussed in the remainder of this section were generated using quasi-stationary SORDUP propagation in the local model with input from the Buoy 51001 model in nonstationary mode with S&L propagation.

[36] Local model predictions were sensitive to directional resolution and particularly spatial resolution of the computation grid (Figures 9, 10, and 11 and Table 3). Considering the complex bathymetry of the bay, it is not surprising that 200 and 100 m spatial resolution grids did not adequately describe propagation patterns and led to poor estimates of H_s within the bay. This is particularly true during the NW swell event; the peak measured H_s at the NW Reef site was underestimated by 2.5 m or more and overestimated at the Wall site (Figure 10). Spatial resolution of 40 m or less performed far better, with successively finer spatial and directional resolutions generally improving comparisons with measurements; the highest-resolution simulations (Δx, Δy = 10 m, $\Delta\theta$ = 1°) modeled refraction of up to 75° at both the NW Reef and Wall sites. Even at this highest of resolutions, the model tended to overestimate wave heights in trade wind conditions (bias ~0.1 m) and underestimate it during NW swell conditions (bias ~−0.3 m, Table 3) This appears to be primarily due to underestimating θ_p, particularly at the NW Reef site during NW swell conditions (Figure 11). The model's poorer performance during the peak of the NW swell may also be partially due to not accounting for current-induced refraction

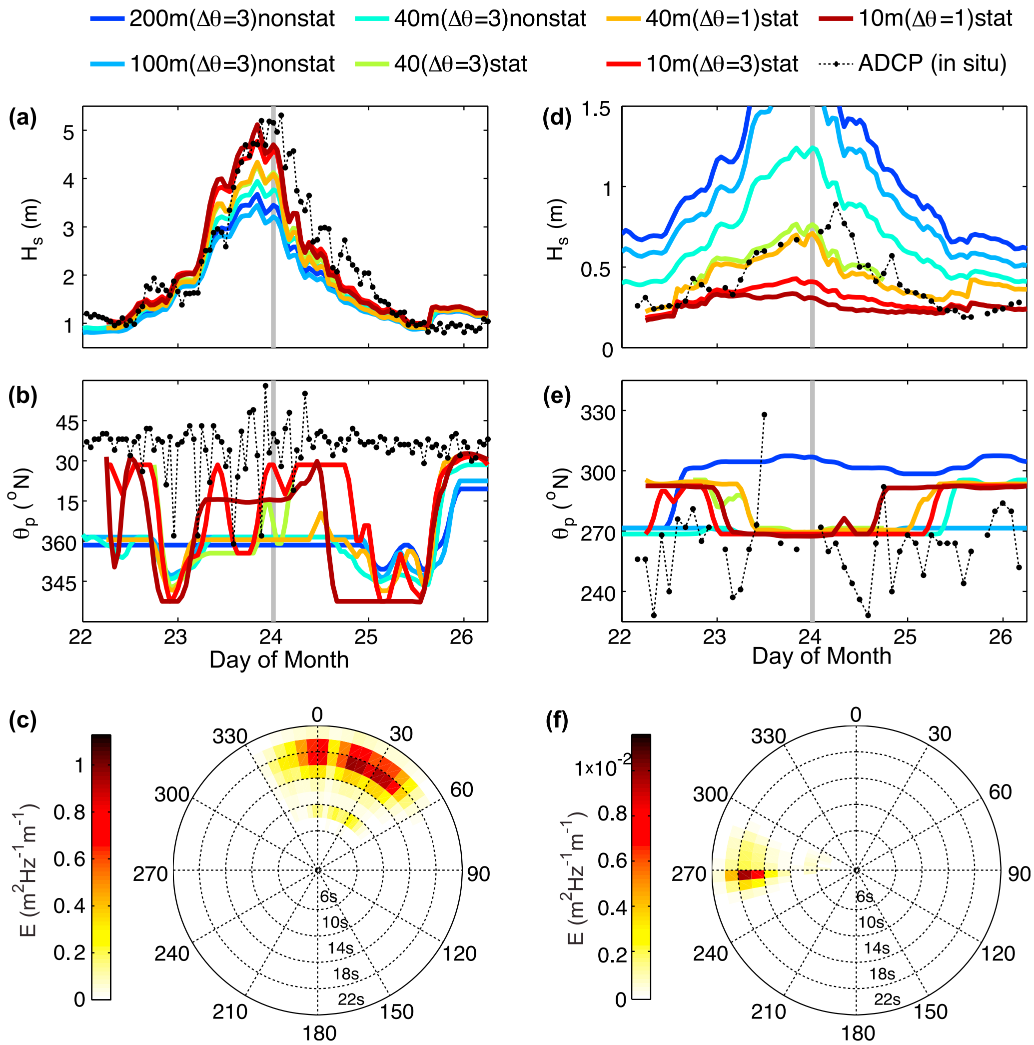

Figure 11. Comparison of varying model simulation resolution and propagation with in situ data during NW swell event, 20–27 January 2006. In the legend, the spatial resolution is given (e.g., 200 m) and the directional resolution in degrees (e.g., $\Delta\theta = 3$) and propagation as nonstat for nonstationary first-order and stat for stationary second-order are defined; if diffraction is included, diff is added. (a) H_s at the NW Reef site. (b) Peak direction (θ_p) at the NW Reef site. (c) NW Reef model spectrum for the highest-resolution run (10 m($\Delta\theta = 3$)stat/diff). (d) H_s at the Wall site. (e) Peak direction (θ_p) at the Wall site. (f) Wall model spectrum for the highest-resolution simulation (10 m($\Delta\theta = 1$)stat/diff). The time of the spectra are indicated with a gray bars in the time series plots.

[*Mulligan et al.*, 2008b]; this effect would be relatively greater during periods of high wave induced current.

[37] The inclusion of phase-decoupled estimated diffraction [*Holthuijsen et al.*, 2003] improved results at the Wall site under trade wind conditions (Figures 9 and 10 and Table 3), indicating diffraction is an important process along the neighboring near-vertical reef slope. Higher-resolution simulations of the NW swell that included diffraction failed to converge. Neglecting diffraction explains poorer model performance under NW swell conditions when the spatial resolution of the model is increased from 40 m to 10 m and directional resolution from $\Delta\theta = 3°$ to 1° for SORDUP propagation cases (in contrast to all other cases, Figure 9). This drop in skill scores is due solely to poorer H_s prediction at the Wall site (higher RMSE and bias). While the more spatially complex estimation of refraction at higher resolution is likely more realistic (H_s prediction is improved at higher resolutions at the NW Reef site), it leads to an underestimation of H_s at the Wall site (Figure 11), presumably because the lateral transfer of wave energy along the crest is neglected.

[38] Varying bottom roughness in the different simulations did not lead to large differences in the results at the more exposed CRAMP and NW Reef site in either trade wind or NW swell conditions (Table 3). Roughness lengths (k_w) of 0.01 and 0.10 m for sand and Reef areas, respectively, generally optimized results at the Wall site; these values for reef are in the range of that found in previous studies [*Hearn et al.*, 2001; *Lowe et al.*, 2005].

[39] The high-resolution simulations focus wave rays in complex patterns during the long wavelengths of the NW swell event: the deeper offshore reef at the mouth of the bay

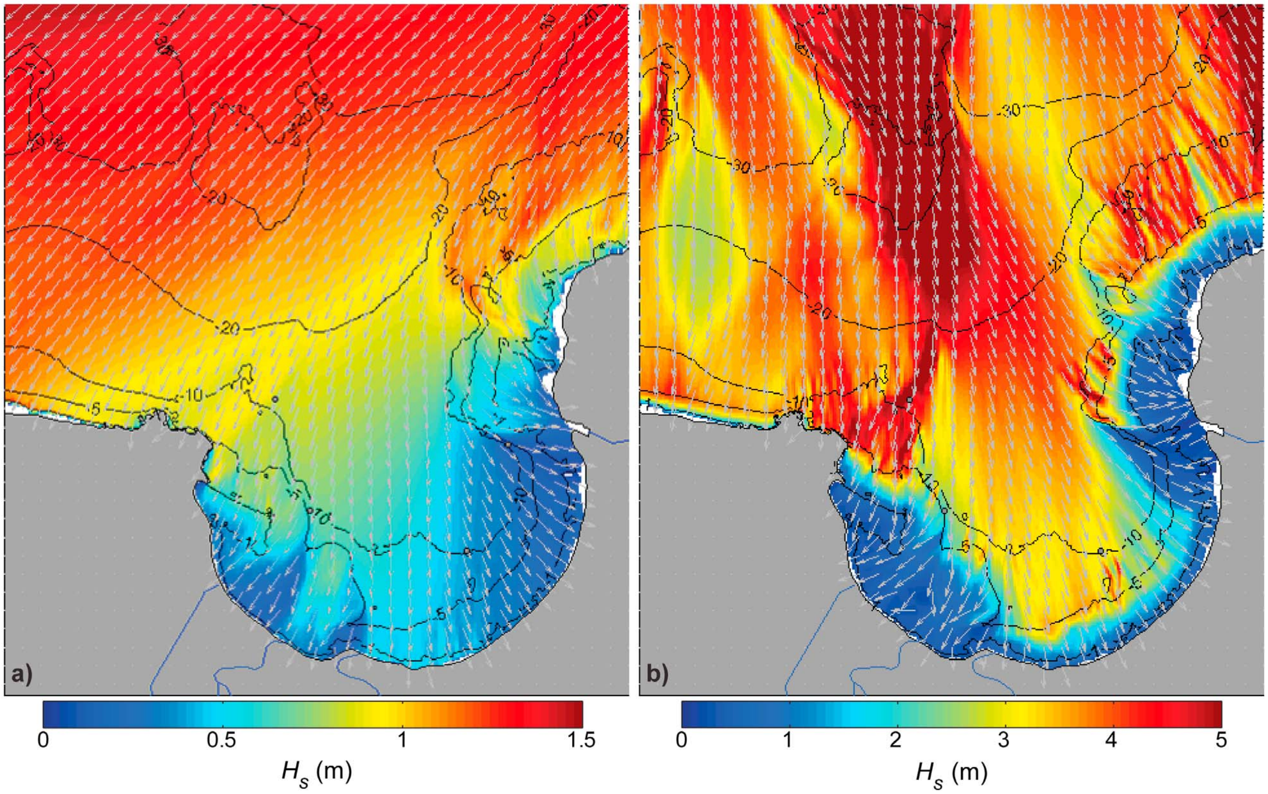

Figure 12. Modeled significant wave height (H_s) with peak direction (θ_p) indicated by arrows. (a) Trade wind conditions (1200 on 5 August 2006) and (b) NW swell event (0600 on 24 January 2007). Note the difference in the color scaling between Figures 12a and 12b.

(King's Reef) can be seen focusing wave energy on fringing reefs on either side of the bay (Figure 12). The NW Reef site appears to be a zone where wave rays coming from directly offshore converge with wave rays refracted over King's Reef, resulting in a split spectrum (Figure 11). There is some evidence for this in the NW Reef observations and may explain why observed H_s at the site approaches or even exceeds offshore H_s, during periods of T_p greater than 15 s.

[40] In both conditions, the fringing reef neighboring the Wall site (Hanalei Reef) is an area of relatively high incident Rave energy and rapid dissipation, resulting in the highest radiation stress gradient within the bay. This corroborates well with the observed relationship between available nearshore wave energy flux and current velocities outlined in section 3.2.

4. Discussion and Conclusions

[41] Unlike more linear barrier type reefs, where the magnitude of flows may be related to incident wave height but overall circulation patterns are essentially similar under varying wave conditions [e.g., *Hench et al.*, 2008; *Lowe et al.*, 2009], the more complex and incised bathymetry of Hanalei Bay gives rise to fundamentally different circulation patterns under different wave conditions.

[42] During trade winds, when little NW swell is present, flows within the bay show mixed influence of winds, tides, and waves. Circulation consists primarily of wind-and-wave (residual) flow around 0.10–0.20 m/s near the surface, and weak, tidally dominated flows at depth ($\ll$0.05 m/s; Figures 4 and 5 and Table 2), possibly with an extremely weak onshore or counterclockwise residual component at depth [*Storlazzi et al.*, 2009]. The (wind-driven) onshore surface component on the western side likely results in counterclockwise return flow along the shoreline (also suggested by *Calhoun et al.* [2002]). These trade wind conditions dominate throughout the year, but particularly in summer. Based on the observed relationship between nearshore wave energy and water flux into the bay, overall flushing times for the bay in these conditions are likely considerably greater than around 40 h.

[43] When NW swells (the most prevalent episodic condition) occur in the fall, winter and spring, wind and tidal forcing are increasingly overshadowed by depth-integrated flows, generally observed to be in the range 0.2–0.7 m/s (Figures 4 and 5 and Table 2). A strong asymmetry along the principal axis of flow is directed into the bay on its eastern side, the result of wave-driven flow across Hanalei Reef, with a return flow out the mouth of the bay, particularly during larger wave events (Figures 5 and 6). This develops an overall picture of strong wave-dominated, clockwise residual flow throughout the water column during NW swell events, although the picture is likely complicated by small-scale, wave-driven circulation cells, unresolved with the limited ADCP data, particularly in the complex topography on the western side of the bay (Queen's Reef). The magnitudes of flows during these events are highly correlated to offshore incident wave energy flux (Figure 6)

and flushing times are likely significantly less than about 14 h, depending on the level of incident wave energy.

[44] These fundamental differences in circulation between the two most commonly occurring wave conditions are due to the propagation of wave energy into the bay's interior during NW swell events. The complex refraction patterns and rapid dissipation of wave energy along the bay's fringing reefs in these conditions result in sharp gradients of radiation stress that drive the observed residual flows (Figure 12). By contrast, the shorter wavelengths associated with trade winds are not significantly refracted by King's Reef and other deeper reef structures; therefore, much less available wave energy, already propagating at a more oblique angle to the coast than NW swells, is refracted into the bay (Figure 12).

[45] The greater vigor of circulation during NW swell events, particularly near the seabed, coupled with the large bed shear stress generated by the near bed orbital velocities associated with the swell propagating into the bay, indicate that these episodic events are a primary driver of sedimentation/erosion, water quality, and benthic ecology. This is evidenced by sediment characteristics within the bay [*Calhoun et al.*, 2002; *Draut et al.*, 2009]; by observations of the resuspension of sediment [*Storlazzi et al.*, 2009]; and by the low reported coral cover on the shallow, exposed forereefs (2–15%) compared to elsewhere in the bay (24–47% of hard bottom substrates [*Friedlander and Brown*, 2005]). Given the low annual number of these NW swell events (on the order of 10 times per year [*Vitousek and Fletcher*, 2008], occurring ~9% of the time) compared to the frequency of modal trade wind conditions (~75% of the time), water quality and sediment and ecosystem dynamics may be sensitive to changes in the magnitude and annual recurrence of these events.

[46] The incised, fringing reef embayment morphology of Hanalei Bay is common to tropical and subtropical high islands in the Pacific, Indian, and Atlantic Oceans. Numerous other examples may be found not only in the Hawaiian Islands, but in the also in the Mascarene Islands, Samoa, and the Caribbean. Similar to the Hawaiian Islands, many of these islands are in the trade wind belt but are exposed to long-period swells generated by (often geographically distant) mid- and high-latitude cyclones, as well as occasional impacts from tropical cyclone waves, as shown by a number of studies of extreme wave events and wave climate [e.g., *Caldwell*, 2005; *Vitousek and Fletcher*, 2008; *Bromirski et al.*, 2005]. However, these studies either neglect wave direction or focus solely on the most extreme events. As evidenced by this study, the degree and frequency with which both these episodic swells and more moderate wind waves may affect circulation, and thus sediment processes and benthic ecosystem dynamics, depends heavily on the degree to which these waves propagate into a particular bay. This in turn depends heavily these waves' dominant direction, the orientation of the coast, and the morphology of the particular bay in question. Thus understanding coastal dynamics where wave-driven flows are important depends heavily on the directional aspect of both modal and episodic wave climate. The methods for producing seasonal directional wave climatologies presented in this paper (Figure 3) are an example interpreting the necessary wave climate information, and are a substantial improvement over the largely qualitative work commonly cited in coastal studies in the Hawaii region [*Moberly and Chamberlain*, 1964].

[47] If wave climate information is to be used to better understand and predict circulation, sediment processes and benthic ecosystem dynamics, then evaluation of existing coastal (shallow water) wave models' ability to accurately predict the propagation of waves into the relatively steeper and more rugose fringing reef embayments from offshore conditions is a prerequisite. The evaluation of the phase-averaged wave model (SWAN) presented here indicates it is capable of performance similar to that considered acceptable (normalized skill of around 0.8) in more linear, lower-sloped continental margin environments [e.g., *Ris et al.*, 1999; *Sutherland et al.*, 2004], provided model resolution is fine enough (Table 3). In this study, minimum acceptable spatial resolution (Δx, Δy) was on the order of 40 m and minimum spectral directional resolution ($\Delta\theta$) was 3°. Further increasing spatial and directional resolution continued to improve performance, however refraction continued to be underestimated during events with larger incident wave heights and periods ($H_s > 2$ m, $T_p > 13$ s), at least to the limit of spatial resolution tested (Δx, Δy = 10 m). The use of unstructured grids (supported by the newest version of SWAN, 40.72) with very high resolution over bathymetrically complex areas was not used in this study but may improve results while keeping computational costs down. Including phase decoupled diffraction [*Holthuijsen et al.*, 2003] also generally improved performance. However, during events with larger incident wave heights and periods ($H_s > 2$ m, $T_p > 13$ s), diffraction was poorly estimated or failed to converge.

[48] It is likely that the numerically efficient phase-averaged approach of SWAN does not adequately describe wave evolution over the steep and highly refractive (and potentially diffractive) environment of Hanalei Bay (and perhaps similar fringing reef embayments) under longer wavelengths. Given the relatively low contribution of local wind generation to the wavefield within the bay and the importance of refraction and diffraction, a phase-resolving, Boussinesq model such as the one outlined by *Madsen et al.* [2006] would likely provide superior estimations of wavefields in the bay. However, to model the entire bay using this approach would come at exceptional computational cost due to the requisite space and time resolutions. Despite the shortcomings of the phase-averaged approach, the analysis presented here shows it is capable of estimating the wavefield, under most conditions, of highly refractive fringing reef systems with slopes on the order of 0.1 to within the accuracy considered acceptable by other studies of lower-sloped environments.

[49] **Acknowledgments.** Many thanks to Kathy Presto (USGS) for help with both field work and analyzing/interpreting much of the in situ data and to Josh Logan (USGS) and Molly Timmers (NOAA/UH) for assisting in field work. Russell Price (NOAA) kindly assisted with optimizing SWAN source code and assisting the computation effort; thanks go to John Rooney (NOAA/UH) and Jonathon Weiss (NOAA/UH) for collecting multibeam bathymetry to supplement existing lidar and multibeam and aggregating the data. Many thanks also to Matt Rosener (Hanalei Watershed Hui) and Carl Berg (formerly Hanalei Watershed Hui) for field support and local knowledge. Thanks to Kevin Wong (NOAA) for support and discussions on content. The constructive comments of Edwin Elias (USGS) on early versions of this manuscript and guidance on numerical modeling issues are greatly appreciated. Mike Field (USGS), Li Erikson (USGS), Rusty

Brainard (NOAA), and Peter Vroom (NOAA/UH) all provided reviews and constructive comments on this manuscript. Amanda Toperoff (NOAA/UH) provided excellent assistance in the preparation of figures. This work was jointly supported by U.S. Geological Survey's Coral Reef Project, NOAA's Coral Reef Conservation Program, and the Australia Institute of Marine Science AIMS at JCU program.

References

Andrews, J. C., and G. L. Pickard (1990), The physical oceanography of coral-reef systems, in *Coral Reefs*, edited by Z. Dubinsky, pp. 11–48, Elsevier, Amsterdam.

Battjes, J. A., and J. P. F. M. Janssen (1978), Energy loss and set-up due to breaking of random waves, paper presented at 16th International Conference Coastal Engineering, Am. Soc. of Civ. Eng., Hamburg, Germany.

Booij, N., R. C. Ris, and L. H. Holthuijsen (1999), A third-generation wave model for coastal regions: 1. Model description and validation, *J. Geophys. Res.*, *104*(C4), 7649–7666, doi:10.1029/98JC02622.

Bromirski, P. D., D. R. Cayan, and R. E. Flick (2005), Wave spectral energy variability in the northeast Pacific, *J. Geophys. Res.*, *110*, C03005, doi:10.1029/2004JC002398.

Caldwell, P. (2005), Validity of North Shore, Oahu, Hawaiian Islands surf observations, *J. Coastal Res.*, *21*, 1127–1138, doi:10.2112/03-0092.1.

Calhoun, R. S., C. H. Fletcher, and J. N. Harney (2002), A budget of marine and terrigenous sediments, Hanalei Bay, Kauai, Hawaiian Islands, *Sediment. Geol.*, *150*, 61–87, doi:10.1016/S0037-0738(01)00268-8.

Callaghan, D. P., P. Nielsen, N. Cartwright, M. R. Gourlay, and T. E. Baldock (2006), Atoll lagoon flushing forced by waves, *Coastal Eng.*, *53*(8), 691–704, doi:10.1016/j.coastaleng.2006.02.006.

Coronado, C., J. Candela, R. Iglesias-Prieto, J. Sheinbaum, M. López, and F. J. Ocampo-Torres (2007), On the circulation in the Puerto Morelos fringing reef lagoon, *Coral Reefs*, *26*(1), 149–163, doi:10.1007/s00338-006-0175-9.

Dean, R. G., and R. A. Dalrymple (1991), *Water Wave Mechanics for Engineers and Scientists*, World Sci, Singapore.

Dollar, S. J. (1982), Wave stress and coral community structure in Hawaii, *Coral Reefs*, *1*(2), 71–81, doi:10.1007/BF00301688.

Draut, A. E., M. H. Bothner, M. E. Field, R. L. Reynolds, S. A. Cochran, J. B. Logan, C. D. Storlazzi, and C. J. Berg (2009), Supply and dispersal of flood sediment from a steep, tropical watershed: Hanalei Bay, Kaua'i, Hawai'i, USA, *Geol. Soc. Am. Bull.*, *121*(3–4), 574–585, doi:10.1130/B26367.1.

Emery, W., and R. Thomson (2001), *Data Analysis Methods in Physical Oceanography*, 2nd ed., 638 pp., Elsevier Sci., New York.

Fabricius, K. E. (2005), Effects of terrestrial runoff on the ecology of corals and coral reefs: Review and synthesis, *Mar. Pollut. Bull.*, *50*(2), 125–146, doi:10.1016/j.marpolbul.2004.11.028.

Field, M. E., C. S. Berg, and S. A. Cochran (2007), Science and management in the Hanalei watershed; a trans-disciplinary approach, *U.S. Geol. Surv. Open File Rep., 2007–1219*, 92 pp.

Friedlander, A. M., and E. K. Brown (2005), Hanalei benthic communities since 1992: Spatial and temporal trends in a dynamic Hawaiian coral reef ecosystem, *Tech. Rep. HCSU-003*, 32 pp., Hawai'i Coop. Stud. Unit, Univ. of Hawai'i at Hilo, Hilo, Hawaii.

Friedlander, A. M., and J. D. Parrish (1997), Fisheries harvest and standing stock in a Hawaiian Bay, *Fish. Res.*, *32*, 33–50, doi:10.1016/S0165-7836(97)00038-6.

Fulton, C. J., and D. R. Bellwood (2005), Wave-induced water motion and the functional implications for coral reef fish assemblages, *Limnol. Oceanogr.*, *50*(1), 255–264, doi:10.4319/lo.2005.50.1.0255.

Gourlay, M. R., and G. Colleter (2005), Wave-generated flow on coral reefs—An analysis for two-dimensional horizontal reef-tops with steep faces, *Coastal Eng.*, *52*(4), 353–387, doi:10.1016/j.coastaleng.2004.11.007.

Grigg, R. W. (1998), Holocene coral reef accretion in Hawaii: A function of wave exposure and sea level history, *Coral Reefs*, *17*(3), 263–272, doi:10.1007/s003380050127.

Hamner, W. M., and E. Wolanski (1988), Hydrodynamic forcing functions and biological processes on coral reefs: A status review, *Proc. Int. Coral Reef Symp.*, *6*(1), 103–113.

Hanson, J. L., B. A. Tracy, H. L. Tolman, and D. Scott (2006), Pacific hindcast performance evaluation of three numerical wave models, paper presented at 9th International Workshop on Wave Hindcasting and Forecasting, Environ. Can., Victoria, B. C., Canada.

Hearn, C. (1999), Wave-breaking hydrodynamics within coral reef systems and the effect of changing relative sea level, *J. Geophys. Res.*, *104*(C12), 30,007–30,019.

Hearn, C., M. Atkinson, and J. Falter (2001), A physical derivation of nutrient-uptake rates in coral reefs: Effects of roughness and waves, *Coral Reefs*, *20*(4), 347–356, doi:10.1007/s00338-001-0185-6.

Hench, J. L., J. J. Leichter, and S. G. Monismith (2008), Episodic circulation and exchange in a wave-driven coral reef and lagoon system, *Limnol. Oceanogr.*, *53*(6), 2681–2694, doi:10.4319/lo.2008.53.6.2681.

Holthuijsen, L. H., A. Herman, and N. Booij (2003), Phase-decoupled refraction-diffraction for spectral wave models, *Coastal Eng.*, *49*(4), 291–305, doi:10.1016/S0378-3839(03)00065-6.

Jokiel, P. L., E. K. Brown, A. Friedlander, S. K. Rodgers, and W. R. Smith (2004), Hawai'i Coral Reef Assessment and Monitoring Program: Spatial patterns and temporal dynamics in reef coral communities, *Pac. Sci.*, *58*, 159–174, doi:10.1353/psc.2004.0018.

Kraines, S., T. Yanagi, M. Isobe, and H. Komiyama (1998), Wind-wave driven circulation on the coral reef at Bora Bay, Miyako Island, *Coral Reefs*, *17*(2), 133–143, doi:10.1007/s003380050107.

Lowe, R. J., J. L. Falter, M. D. Bandet, G. Pawlak, M. J. Atkinson, S. G. Monismith, and J. R. Koseff (2005), Spectral wave dissipation over a barrier reef, *J. Geophys. Res.*, *110*, C04001, doi:10.1029/2004JC002711.

Lowe, R. J., J. L. Falter, S. G. Monismith, and M. J. Atkinson (2009), Wave-driven circulation of a coastal reef-lagoon system, *J. Phys. Oceanogr.*, *39*, 873–893, doi:10.1175/2008JPO3958.1.

Luketina, D. (1998), Simple tidal prism models revisited, *Estuarine Coastal Shelf Sci.*, *46*(1), 77–84, doi:10.1006/ecss.1997.0235.

Lygre, A., and H. E. Krogstad (1986), Maximum entropy estimation of the directional distribution in ocean wave spectra, *J. Phys. Oceanogr.*, *16*, 2052–2060, doi:10.1175/1520-0485(1986)016<2052:MEEOTD>2.0.CO;2.

Madin, J. S., and S. R. Connolly (2006), Ecological consequences of major hydrodynamic disturbances on coral reefs, *Nature*, *444*, 477–480, doi:10.1038/nature05328.

Madsen, O. S., Y.-K. Poon, and H. C. Graber (1988), Spectral wave attenuation by bottom friction: Theory, paper presented at 21st International Conference on Coastal Engineering, Am. Soc. of Civ. Eng., Torremolinos, Spain.

Madsen, P. A., D. R. Fuhrman, and B. Wang (2006), A Boussinesq-type method for fully nonlinear waves interacting with a rapidly varying bathymetry, *Coastal Eng.*, *53*(5–6), 487–504, doi:10.1016/j.coastaleng.2005.11.002.

Massel, S. R., and M. R. Gourlay (2000), On the modelling of wave breaking and set-up on coral reefs, *Coastal Eng.*, *39*(1), 1–27, doi:10.1016/S0378-3839(99)00052-6.

Moberly, R., and T. Chamberlain (Eds.) (1964), Hawaiian Beach Systems, *Hawai'i Inst. Geophys. Rep. 64–2*, 42 pp., Univ. of Hawai'i at Mānoa, Honolulu.

Monismith, S. G. (2007), Hydrodynamics of coral reefs, *Annu. Rev. Fluid Mech.*, *39*(1), 37–55, doi:10.1146/annurev.fluid.38.050304.092125.

Mulligan, R. P., A. J. Bowen, A. E. Hay, A. J. d. Westhuysen, and J. A. Battjes (2008a), Whitecapping and wave field evolution in a coastal bay, *J. Geophys. Res.*, *113*, C03008, doi:10.1029/2007JC004382.

Mulligan, R. P., A. E. Hay, and A. J. Bowen (2008b), Wave-driven circulation in a coastal bay during the landfall of a hurricane, *J. Geophys. Res.*, *113*, C05026, doi:10.1029/2007JC004500.

Munk, W. H., and M. C. Sargent (1954), Adjustment of Bikini Atoll to ocean waves, *U.S. Geol. Surv. Prof. Pap., 260-C*, 280 pp.

National Marine Fisheries Service (2006). NOAA Ship Hi'ialakai, *Cruise Rep. CR-07–004*, 142 pp., Pac. Isl. Fish. Sci. Cent., Honolulu.

Pawlowicz, R., B. Beardsley, and S. Lentz (2002), Classical tidal harmonic analysis including error estimates in MATLAB using T_TIDE, *Comput. Geosci.*, *28*(8), 929–937, doi:10.1016/S0098-3004(02)00013-4.

Ris, R., L. Holthuijsen, and N. Booij (1999), A third-generation wave model for coastal regions: 2. Verification, *J. Geophys. Res.*, *104*(C4), 7667–7681, doi:10.1029/1998JC900123.

Rogers, C. S. (1993), Hurricanes and coral reefs: The intermediate disturbance hypothesis revisited, *Coral Reefs*, *12*(3–4), 127–137, doi:10.1007/BF00334471.

Rogers, W. E., J. M. Kaihatu, H. A. H. Petit, N. Booij, and L. H. Holthuijsen (2002), Diffusion reduction in an arbitrary scale third generation wind wave model, *Ocean Eng.*, *29*(11), 1357–1390, doi:10.1016/S0029-8018(01)00080-4.

Rooney, J. J. B., and C. H. Fletcher (2005), Shoreline Change and Pacific Climatic Oscillations in Kihei, Maui, Hawaii, *J. Coastal Res.*, *21*, 535–547, doi:10.2112/03-0077.1.

Singamsetti, S. R., and H. G. Wind (1980), Breaking waves; characteristics of shoaling and breaking periodic waves normally incident to plane beaches of constant slope, *Rep. M1371*, 80 pp., Delft Hydraulics, Delft, Netherlands.

Storlazzi, C. D., A. S. Ogston, M. H. Bothner, M. E. Field, and M. K. Presto (2004), Wave- and tidally driven flow and sediment flux across a fringing coral reef: Southern Molokai, Hawaii, *Cont. Shelf Res.*, *24*(12), 1397–1419, doi:10.1016/j.csr.2004.02.010.

Storlazzi, C. D., E. K. Brown, M. E. Field, K. Rodgers, and P. L. Jokiel (2005), A model for wave control on coral breakage and species distribution in the Hawaiian Islands, *Coral Reefs*, *24*(1), 43–55, doi:10.1007/s00338-004-0430-x.

Storlazzi, C. D., M. K. Presto, J. B. Logan, and M. E. Field (2006), Coastal circulation and sediment dynamics in Hanalei Bay, Kauai. Part I: Measurements of waves, currents, temperature, salinity and turbidity: June–August, 2005, *U.S. Geol. Surv. Open File Rep., 2006–1085*, 35 pp.

Storlazzi, C. D., M. K. Presto, J. B. Logan, and M. E. Field (2008), Coastal circulation and sediment dynamics in Hanalei Bay, Kaua'i, Part IV: Measurements of waves, currents, temperature, salinity, and turbidity, June–September 2006, *U.S. Geol. Surv. Open File Rep., 2006–1085*, 29 pp.

Storlazzi, C. D., M. E. Field, M. H. Bothner, M. K. Presto, and A. E. Draut (2009), Sedimentation processes in a coral reef embayment: Hanalei Bay, Kauai, *Mar. Geol.*, *264*(3–4), 140–151, doi:10.1016/j.margeo. 2009.05.002.

Sutherland, J., A. H. Peet, and R. L. Soulsby (2004), Evaluating the performance of morphological models, *Coastal Eng.*, *51*(8–9), 917–939, doi:10.1016/j.coastaleng.2004.07.015.

Tolman, H. L. (2002), User manual and system documentation of WAVEWATCH-III version 2.22, *Tech. Note 222*, 133 pp., NOAA, Natl. Cent. for Enivorn. Predict., Washington, D. C.

Vitousek, S., and C. H. Fletcher (2008), Maximum annually recurring wave heights in Hawai'i1, *Pac. Sci.*, *62*, 541–553, doi:10.2984/1534-6188(2008)62[541:MARWHI]2.0.CO;2.

von Arx, W. S. (1954), Circulation systems of Bikini and Rongelap lagoons, *U.S. Geol. Prof. Pap., 260-B*, 273 pp.

Willmott, C. J., R. E. Davis, J. J. Feddema, K. M. Klink, D. R. Legates, C. M. Rowe, S. G. Ackleson, and J. O'Donnell (1985), Statistics for the evaluation and comparison of models, *J. Geophys. Res.*, *90*(C5), 8995–9005, doi:10.1029/JC090iC05p08995.

Wolanski, E., R. H. Richmond, G. Davis, and V. Bonito (2003), Water and fine sediment dynamics in transient river plumes in a small, reef-fringed bay, Guam, *Estuarine Coastal Shelf Sci.*, *56*(5–6), 1029–1040, doi:10.1016/S0272-7714(02)00321-9.

R. Hoeke, Joint Institute for Marine and Atmospheric Research, University of Hawai'i at Mānoa, 1125B Ala Moana Blvd., Honolulu, HI 96814, USA. (hoeke@hawaii.edu)

P. Ridd, School of Engineering and Physical Sciences, James Cook University, Townsville, Qld 4811, Australia.

C. Storlazzi, Coastal and Marine Geology Program, U.S. Geological Survey, 400 Natural Bridges Dr., Santa Cruz, CA 95060, USA.